Hydrodynamics of a hyper-tidal estuary influenced by the world's second largest tidal power station (Rance estuary, France)

Rajae Rtimi, Aldo Sottolichio, Pablo Tassi

Version of Record: https://www.sciencedirect.com/science/article/pii/S027277142030874X
Manuscript_eac92808fae6ceac2b049f5cbcb794a4

Hydrodynamics of a hyper-tidal estuary influenced by the world's second largest tidal power station (Rance estuary, France)

Rajae RTIMI[1,2], Aldo SOTTOLICHIO[2], and Pablo TASSI[1,3]

[1]Electricité de France, Research and Development Departement (EDF R&D). Address: 6 Quai Watier, 78400 Chatou, France. Email: rajae.rtimi@edf.fr; pablo.tassi@edf.fr

[2]EPOC Laboratory CNRS, University of Bordeaux. Address: Allée Geoffroy Saint Hilaire, 33615 Pessac, France. Email: aldo.sottolichio@u-bordeaux.fr

[3]Saint-Venant Hydraulics Laboratory. Address: 6 Quai Watier, 78400 Chatou, France.

Abstract

The Rance estuary is a relatively small low-discharge steep-sided *ria*, located along the Brittany coast in northern France, with a maximum spring tidal range of 13.5 m. Taking advantage of this hyper-tidal regime, the first and currently the second largest operational tidal power station in the world was built at the estuary's mouth and has been in operation since the 1960s. Despite the well-known effect of damping of estuarine water levels, little attention has been given to quantifying the influence of the plant on the propagation and asymmetry of the tidal wave inside the estuary. In this study, hydrodynamics and tidal wave patterns were analyzed in this anthropogenically influenced estuarine system. A two-dimensional depth-averaged numerical model of the Rance estuary was developed. Two scenarios without the tidal power plant involving the dam's pre- and post-construction bathymetry (1957 and 2018 respectively) and present-day conditions scenarios were designed, to highlight the impact of bed evolution and the tidal power station on hydrodynamics and tidal asymmetry. Numerical results showed that, without the structure, bathymetric evolution did not substantially influence estuarine hydrodynamics. Nevertheless, on the estuary-side of the dam, the presence of the tidal power plant induced (i) a decrease in both tidal range and tidal prism, (ii) an increase of low water levels, and (iii) a decrease in both flood and ebb currents. Contrastingly, the region close to the structure reacted differently to plant operating modes, with an increase in flood currents (ebb currents) upstream of

the sluice gates (downstream of the turbines). For both the natural condition and the artificially-induced hydrodynamic forcing due to the presence of the plant, numerical results showed that the Rance estuary mainly exhibits flood-dominant behavior, with a longer duration of falling than rising water and stronger peak flood currents than ebb currents. Spanning a period of approximately 60 years, this study presents a quantitative analysis of the influence of the tidal power station on the hydrodynamics in the Rance estuary, and its possible consequences for sediment dynamics. This approach is novel for this particular enclosed water body, characterized by the presence of a dam at its mouth and a lock at its uppermost limit.

Keywords: Tidal power station, Rance estuary, hydrodynamic processes, tidal asymmetry, numerical modeling.

1 Introduction

Hyper-tidal estuaries exhibit large tidal range (i.e., mean tidal range>6 m) and strong tidal currents, making them ideal for tidal renewable energy projects. Tidal energy is a form of hydro-power with potential as one of the future sources of renewable energy. However, a tidal power project can modify local hydrodynamics significantly, with impact on sediment dynamics, water quality and ecosystems [1, 2, 3]. Therefore, understanding the impact on hydrodynamics induced by tidal projects is crucial for predicting possible environmental impacts.

In estuaries, hydrodynamic behavior is influenced by several factors [4, 5, 6, 7]: (i) the gravitational forces of the Moon and the Sun combined with the rotation of the Earth; (ii) the estuary's morphology, and (iii) the freshwater input discharge. In macro-tidal estuaries, hydrodynamics is mainly governed by tides which, have a profound impact on residual sediment dynamics and consequently on morphological evolution [8]. As examined by several authors [9, 10, 11, 12, 13], tidal asymmetry plays an important role, causing residual sediment transport in estuarine systems [14, 15, 16], and can be computed from flow velocity and water elevation [11, 12, 17]. The former identifies the nature of the asymmetry: *i.e.,* ebb- or flood-dominance in the estuary. The latter compares the durations of rising and falling tides. This indicates the predominant direction of residual transport of coarse sediment (gravel and sand) carried by bedload and of fine sediment (silt and clay) carried by suspension. Asymmetry in low and high slack water duration is also relevant to the net transport of the finer sediment fraction in the water column [18]. A human intervention such as a dam located at a seaward boundary modifies the hydrodynamic regime and significantly alters non-linear

tidal interactions [9, 10, 19, 20], which can be relevant to sediment transport and accumulation in highly anthropized estuarine systems.

Located on the Brittany coast of northern France (Figure 1.a), the Rance estuary is a relatively small steep-sided, 20 km long *ria* [21]. Its maximum perigean spring tidal range reaches 13.5 m at the mouth (Saint Servan, Figure 1.b). Taking advantage of this hyper-tidal regime, the first ever tidal power station in the world was built at the estuary mouth (Figure 1.b). The plant has been in operation and managed by Electricité de France (EDF) since 1966 and is currently the second largest operational tidal power station in the world [22]. With a peak (mean) output capacity of 240 MW (57 MW), it supplies 0.12% of the power demand in France, which is equivalent to a medium-size city such as Rennes (*c.* 225,000 in habitants) [23].

Experimental and numerical studies were conducted, mainly focusing on qualitative analysis of sediment dynamics or ecosystem evolution in the estuary, without prior investigation of how hydrodynamics was influenced by the tidal barrier [3, 24, 25, 26, 27]. Despite a well-known effect on estuarine water levels [24], little attention has been given to quantifying the influence of the plant on the propagation, and vertical and horizontal tidal asymmetry of the tidal wave. The first numerical hydrodynamic model of the Rance estuary was developed in 2001 [26]. It consisted in a two-dimensional (2D) model used to separately study the sea-side and estuary-side regions of the dam. The aim was to determine hydrodynamic parameters for morphological simulations [27]. Although it provided good results with respect to measurements [26], the approach did not evaluate the influence of the power plant on flow characteristics and tidal asymmetry, which could have significant implications for sediment dynamics and morphological changes in the estuary. In 2018, 2D and 3D numerical models were developed, to evaluate bacteriological impact in the estuary [28]. The study area included both the basin and the offshore region. However, mesh resolution was constant over the computational domain, which was insufficient to capture flow structure close to the plant and between Mordreuc and Chatelier lock (Figure 1.b). The main conclusions of this study were based on the 2D model results, without any further hydrodynamic analysis.

Both 2D and 3D numerical models are used to assess hydrodynamic impacts of existing or planned tidal power plant projects. With the third highest tidal range in the world (15m maximum in spring tide), the Severn estuary (United Kingdom) would be an optimal location for tidal power projects. A 2D numerical model was developed by [1] to estimate the impact of three renewable-energy projects: Cardiff–Weston, Fleming lagoon and Shoots dams. The basic dam operation regime adopted was ebb generation only. It was concluded that the Fleming Lagoon project would have little influence on hydrodynamic processes in

the Severn estuary, however dam construction would have significant environmental impact [1]. Young *et al.* developed a 2D hydrodynamic model to highlight the impact of the world's largest tidal power station, the Sihwa Lake tidal power plant in South Korea [29]. The tidal energy scheme of this plant is a single flood-generation mode. The study established that limiting water surface elevation would modify the estuary's ecosystem [29]. Another optimal location for a tidal power plant would be the Bay of Fundy, located on the Atlantic coast of North America, where tidal range can exceed 16 m during spring tides. 2D and 3D hydrodynamic models [30, 2] simulated a range of hypothetical development scenarios with three different operating modes: ebb generation only, flood generation only, and ebb-flood generation. It was concluded that operating mode had considerable influence on local velocities near the lagoon, and particularly near the powerhouse, but seemed to have little influence on the magnitude of far-field hydrodynamic impact [30, 2]. One common feature of these studies was that they were all conducted ahead of plant construction, and consequently the impact assessments were only estimations.

The main objective of this paper is to analyze how the hydrodynamics of the Rance estuary is influenced by the world's second-largest tidal power station through basic flow characteristics and tidal asymmetry [12, 11]. For this, a two-dimensional depth-averaged model was developed corresponding to both ebb generation and flood-ebb generation schemes (section 3). The numerical model was first calibrated and validated on measurement datasets (section 4.1) and then employed to assess present-day hydrodynamic conditions in the Rance estuary (section 4.2). Application of the numerical model on diverse scenarios involving past/present bed elevations and presence/absence of the dam analyzed the impact of the plant on flow patterns and tidal asymmetry (section 4.3). Finally, section 5 discusses the impact of the Rance tidal power station on hydrodynamic processes and its potential impact on sediment dynamics.

2 Study area

2.1 Rance tidal power station

The main characteristics of the Rance tidal power plant are as follows (Figure 1.c): (i) a 65 m lock, with 20,000 vessels per year passing through; (ii) 24 Kaplan bulb turbines appropriate for very low head and high flow rates [31], 323 m long and 33 m wide, each unit producing 10MW; (iii) a rockfill dyke 165 m long; (iv) 6 sluice gates composing 114x15 m dam; and (v) a road on which 30,000 (60,000 in summer) vehicles per day travel between the cities of Dinard and Saint Malo. The particularity of the Rance tidal power plant is

its ability to produce electricity during both falling and rising tides (Figures 1.d & 1.e), operating by one- and two-way generation modes thanks to the capacity of its Kaplan bulb turbines to rotate in both directions [32, 29]. The Rance River drains a small catchment area, with an average river discharge of 7 m^3/s, low water flow rate of 0.5 m^3/s and a decennial flood of 80 m^3/s. These magnitudes are small compared to the tidal flux observed upstream of the plant, with about 9,000 m^3/s maximum in neap tide and 18,000 m^3/s in spring tide (Figure 1.b). Further information on the estuary's morphology, sedimentary and hydrological characteristics can be found in [24].

2.2 Evolution of bed elevation between 1957 and 2018

During the last 58 years, between 1960 (before plant construction) and 2018, the Rance estuary has been subject to natural and artificial sedimentary processes governing its morphological evolution. In the present study, two bathymetry configurations were used for digital elevation models (DEMs), corresponding to the available datasets. The first DEM corresponds to the year 1957, prior to the plant's construction (Figure 2.a), and the second to the year 2018, which is the most recent bathymetric survey (Figure 2.b). For both 1957 and 2018 datasets, spatial coordinates were expressed according to the World Geodetic System 1984 (WGS84). Altitude was adjusted to the zero-level provided by the National Hydrograph Service (chart datum).

Bathymetry for 1957 was reconstructed using historical maps and data surveyed by EDF, consisting of isobaths and echo-sounder point data at specific locations. To build the Digital Elevation Model, isobaths and point data were vectorized using Global Mapper® and projected in 3D by TerraModel®. The estimated horizontal and vertical uncertainties were of the order of 1m and 0.1m, respectively [33].

From May 29 to June 6 2018, a field survey was carried out to collect bathymetric and topographic data in the estuary. High-frequency multibeam echo-sounder measurements were performed to map the estuary bottom. Intertidal zone topography was measured on a light detection and ranging system (LIDAR) [34]. The mean uncertainties of the horizontal and vertical measurements were of the order of 0.01m.

Downstream of the tidal power station, both DEMs employed the same bathymetry, extracted from the SHOM HistoLitt® surveys carried out between 1970 and 2005 [35]. For seabed depths up to 50m, vertical resolution ranged from 0.3m to 1m and horizontal resolution from 1m to 20m. Beyond 50m, vertical resolution ranged from 1% to 2% of depth and horizontal resolution was few tens of meters [35].

According to bed evolution depicted in Figure 2.c, there was an erosional zone upstream of the sluice gates. Conversely, in the lower part of the estuary, sediment accretion occured in the meandering reach downstream

of Mordreuc. Furthermore, in the middle-estuary region between Ton peak and Saint Hubert port, little difference was observed between the 1957 and 2018 bathymetries. The changes in bathymetry may present inaccuracies due to measurement uncertainty in the older maps.

3 Numerical modeling

3.1 Hydrodynamic model

The TELEMAC-2D module, belonging to the open-source TELEMAC-MASCARET modeling system (www.opentelemac.org) was used to study hydrodynamics in the Rance estuary and to investigate changes in flow characteristics induced by the tidal power plant. This module solves the two-dimensional, horizontal shallow water equations (2DH), which implicitly assume hydrostatic pressure distribution, constant fluid density and depth-averaged velocity components [36, 37]. This modeling approach has been applied to other shallow and vertically well-mixed estuaries [38, 39, 40, 41, 2]. The numerical tool has been assessed in applications in several coastal and estuarine cases [42, 43, 44, 45, 46]. Two relationships were specified to close the governing equations: a classical squared function dependency on depth-averaged velocity for bed resistance, and the Boussinesq approximation for turbulence parameterization [36]. This study used the Strickler law for bottom friction and a zero-equation turbulence model with constant eddy viscosity. The Strickler coefficient and eddy viscosity values were assumed to be constant over the whole computational domain. They were calibrated using Acoustic Doppler Current Profiler (ADCP) observed data from 2012 [47] and validated with measurements of water surface elevation from tidal gauges during 2019. The computational domain covered the sea-side and the estuary-side areas extending from the oceanic open boundary ($\sim$ 20km from the tidal power plant) to the upstream limit (Chatelier lock). It was discretized with an unstructured mesh generated by the BlueKenue® pre- and post-processing tool [48]. The mesh consisted of 399, 512 triangular elements and 204, 565 nodes with variable resolution ranging between 1000m offshore, 250m near the coastline, 50m around the estuary mouth, 20m inside the estuary and 5m close to power station and within the lower estuary between Mordreuc and Chatelier lock, see Figure 1 [49]. The topo-bathymetric information contained in the DEM was projected onto the finite element mesh using the inverse distance weighting interpolation algorithm [50]. Boundary conditions were set as follows:

(i) At the oceanic open boundary (offshore), water levels and velocity component values were imposed

through 11 tidal constituents (M2, S2, N2, K2, K1, O1, P1, Q1, M4, MS4 and MN4) from the OSU TPXO European Shelf 1/30 regional model [51].

(ii) At the upstream limit (Chatelier lock, Figure 1), freshwater input from the Rance river was set up as varying between $5m^3/s$ and $30m^3/s$. The configuration of this boundary is complex: in addition to the lock, 2 sluice gates maintain constant water level at the port located upstream of the Chatelier lock. As the flow passing through these structures is not measured, flow discharge was estimated from the mean Rance river flowrate, collected from the nearest hydrometric station located ~ 33km upstream of Chatelier lock.

(iii) The tidal power station was represented by two weirs: the first depicts the turbines structure and the second depicts the sluice gates structure. Unlike existing tidal power station models (TPS models) [52, 2, 1], the operation modes of the turbines and sluice gates were calculated by an external optimization algorithm Software named AGRA [53] and not by the head difference seen on TELEMAC-2D. AGRA Software, based on the dynamic programming method [54], is used by operators in charge of the plant to simulate optimal energy generation and the resulting hydraulic conditions (flowrates, start and stop times, *etc*.), notably according to head difference and equipment availability [53]. In order to be consistent with the actual regime of the power plant, the AGRA output was used as input in the TELEMAC-2D model to define the operating mode of the turbines and sluice gates. Following studies by [1, 2, 52], the turbines and sluice gates were treated separately with their corresponding flowrates, to ensure good representation of the complex flow structure in the zone around the dam; the approach of imposing a single flowrate throughout the whole plant boundary was not adopted. In TELEMAC-2D, a weir is considered as a linear singularity, represented by an island in the mesh [55]. Standard weir discharge equations already exist in TELEMAC-2D [55], but were adjusted as follows to suit the Rance tidal plant's operation:

- Flowrate through turbines was computed by three methods depending on operating mode: (a) For direct-, inverse-turbining and direct pumping (D.T., I.T. and D.P. in Table 1), flowrate was interpolated using discharge data generated by the AGRA Software, based on hill charts where flowrate is computed according to turbine blade incidence, which in turn depends on real head difference and tidal power. (b) For filling and draining phases (F.O. and D.O. in Table 1), flowrate $Q_{turbines}$ was computed according to standard orifice equation 1. (c) For Turbines Off phase

(T.O. in Table 1), flowrate $Q_{turbines}$ was set to 0.

$$Q_{turbines} = N_{turb} \cdot A(|\zeta_{estuary} - \zeta_{sea}|)^{1/2} \quad (1)$$

- Flowrate through sluice gates in the Gates Open stage (G.O. in Table 1) was computed by equation 2, adjusted from the standard orifice equation ($Q \propto C_d H^{0.5}$) using a variable instead of a constant discharge coefficient. This approach was adopted since the sluice gates in the Rance power plant are large and appropriate for low head differences, and thus the discharge coefficient varies significantly according to downstream water level. For the Gates Closed stage (G.C, Table 1), flowrate $Q_{sluices}$ was set to 0.

$$Q_{sluices} = N_{sg}(B\zeta_{downstream}^{1/4} - C)(|\zeta_{estuary} - \zeta_{sea}|)^{1/2} \quad (2)$$

In the above equations, $\zeta_{estuary}$ and ζ_{sea} are surface water elevations at Saint Suliac and Saint Servan respectively (see Figure 1 for locations). N_{turb} and N_{sg} are numbers of available turbines and sluice gates respectively. A, B and C are discharge coefficients and $\zeta_{downstream}$ is downstream water surface elevation. Table 2 summarizes values of these parameters (A, B, C, $\zeta_{downstream}$) according to tidal phase (flood and ebb).

Turbine flowrate, $Q_{turbines}$, was then distributed homogeneously across the 24 turbines. Likewise, for sluice gates, $Q_{sluices}$ was distributed homogeneously across the 6 sluice gates. This assumes that all the plant's equipment is available, which is not always the case. However, given that the outage rate for hydroelectric units is low, this assumption would not significantly influence the numerical results. In this study, both water surface elevation and bottom elevation are relative to the chart datum.

(iv) The rest of the domain contour was represented by a closed solid boundary.

3.2 Tide analysis

To analyze in depth the influence of the plant on the hydrodynamics in the estuary, four complementary metrics were evaluated:

(i) Tidal prism (TP), defined as the volume of water leaving the estuary at ebb tide [56]. This parameter was deduced from flowrate passing through the TPS section ($Q_{\sum_{TPS}}$) located upstream of the plant

(Figure 1.b) and was calculated from Eq.3:

$$TP = \int_{t \in ebb} Q_{\sum TPS}(t)\, \mathrm{d}t \tag{3}$$

Tidal prism was further analyzed over a fortnightly tidal cycle to assess its evolution over neap/spring tidal periods.

(ii) Mean residence time (T_r), defined as the time taken by a water parcel to leave a defined region through its outlets to the sea [57]. Following studies by [58, 59, 60], mean residence time can be computed from the theoretical tidal prism method as in Eq.4:

$$T_r = \frac{VT}{(1-b)TP} \tag{4}$$

where V is the mean volume of water in the system, T is the tidal period, TP is the tidal prism, and b is the return-flow factor, defined as the fraction of ebb water returning to the system during the flood tide ($0 < b < 1$) [58].

(iii) Ebb/flood tidal current asymmetry $\gamma_0(n = u)$, and tidal duration asymmetry $\gamma_0(n = \frac{\partial \zeta}{\partial t})$, were quantified by computation of skewness as defined by Nidzieko & Ralston [12]:

$$\gamma_0(n) = \frac{\mu_3(n)}{\mu_2^{3/2}(n)} \tag{5}$$

where the m-th moment about zero, μ_m, is:

$$\mu_m(n) = \frac{1}{N-1} \sum_{i=1}^{N} n_i^m \tag{6}$$

and N is the number of samples n_i and ζ is the water surface elevation.

The Rance estuary does not have a single along-channel velocity direction. For instance, the flow is mainly aligned north-south upstream of Ton peak, and east-west downstream. Hence, the current field can be defined as the velocity magnitude affected by the sign of the North-South velocity component. Parameters ($\gamma_0(u)$;$\gamma_0(\partial\zeta/\partial t)$) were computed as the median over a neap-spring tidal period to analyze their spatial distribution upstream and downstream of the plant;Nidzieko & Ralston [12] showed that

the tide is ebb dominant for $\gamma_0(u) < 0$ and flood dominant for $\gamma_0(u) > 0$. They reported that the duration of falling water is shorter than rising water for $\gamma_0(\frac{\partial \zeta}{\partial t}) < 0$ and longer for $\gamma_0(\frac{\partial \zeta}{\partial t}) > 0$.

(iv) Asymmetry metrics were analyzed by computing the amplitude ratio $\alpha = a_{M_4}/a_{M_2}$ and phase difference $\beta = 2\phi_{M_2} - \phi_{M_4}$ on both water surface elevation (ζ) and current (u). As the Rance estuary is dominated by the $M2$ semidiurnal tide, this approach is appropriate for quantifying tide asymmetry. According to Friedrichs & Aubrey [11], the amplitude ratio α indicates the degree of non-linearity: *i.e.,* the capacity of the estuary to generate/amplify secondary harmonics (M4, M6, *etc*). As for phase difference β, it illustrates the asymmetry direction, flood or ebb dominance. Least squares harmonic analysis of water surface elevation and current was performed on a record of 20 days using the T-TIDE toolbox [61]. Asymmetry metrics were then computed at selected locations in the estuary and further analyzed with Nidzieko & Ralston [12] asymmetry parameters ($\gamma_0(u)$;$\gamma_0(\partial\zeta/\partial t)$).

4 Results

In this section, the numerical model was calibrated and validated using respectively ADCP measurements collected for five tide cycles in 2012 and a water level dataset recorded from tidal gauges for a period of a fortnight in 2019 (subsection 4.1). Numerical model results were then analyzed to better understand the hydrodynamics in the estuary and to highlight the influence of the power plant on the estuarine system. Subsection 4.2 provides a description of the hydrodynamics in the estuary today. Tide propagation and asymmetry are analyzed for three scenarios in subsection 4.3.

4.1 Model calibration and validation

To calibrate the numerical model and validate its capacity to predict water surface elevation and tidal currents, two datasets from 2012 [47] and 2019 were used. Firstly, the numerical model with the recent bathymetry of 2018 (Figure 2), was calibrated using a dataset consisting of Acoustic Doppler Current Profiler (ADCP) measurements for five tide cycles (June 4 – 6 2012) collected at three locations near the power station: upstream of the turbines (ADCP 1), upstream of the sluice gates (ADCP 2) and downstream of the power station (ADCP 3). Secondly, the numerical model was validated using a larger dataset of water surface measurements from tidal gauges for the period August 15 – 28 2019. This validation was needed to assess the capacity of the model to propagate the tide along the estuary from upstream (Chatelier Lock) to mouth

(Saint Servan), over a continuous period of a fortnight. For velocity validation, Root Mean Square Error (RMSE) on current magnitude and direction was calculated. To validate water surface elevation, RMSEs were computed on the entire water-level signal, at high- and low-water levels. Since the model was further used for harmonic analysis, water level validation was complemented by error computation on the amplitude and phase of the M2 and M4 tide constituents.

4.1.1 Model calibration and validation for the year 2012

Imposing a Strickler coefficient of 60 $m^{1/3}/s$ and constant eddy viscosity of 10^{-4} m^2/s over the whole computational domain, numerical results were compared with ADCP measurements at three locations indicated in Figure 3. As shown in Figures 3.a;b;c, the model effectively reproduced water surface elevation with RMSE $\approx$ 8 cm upstream of the TPS and $\approx$ 5 cm downstream (Table 3). High- and low-water levels are also effectively computed by the model with RMSE below 4 cm upstream of the dam and 3 cm downstream of the structure (Table 3). For both stations upstream of the TPS (ADCP1 and ADCP2), high-frequency oscillations of the order of $\sim$ 10cm are clearly seen at low and high water, and the tidal range is approximately 50% less than in the station downstream of the TPS. The numerical model effectively represented water-level oscillations and tidal wave damping inside the estuary caused by the operation of the TPS. It is also able to reproduce satisfactorily velocity magnitude and direction at the three ADCP locations, with RMSE values below 0.2 m/s for current magnitude and 12° for current direction, as shown in Figures 3.d-i) and Table 3. Upstream of the turbines and downstream of the TPS, flood-currents are stronger than ebb-currents, while they are equivalent upstream of the sluice gates. For the latter, the velocity magnitude decreases by 15% and 6% during flood and ebb respectively with respect to velocity magnitude in the sea-side of the dam. However, this reduction is greater upstream of the turbines (ADCP 1), at 48% and 62% for flood and ebb currents respectively. The flood-current measurements exhibited a peak at the beginning of the flood, which is clearer at stations ADCP 2 and ADCP 3 (Figures 3.e;f). The peak upstream of the plant, directly related to turbine operation, is well represented by the numerical model. However, the peak observed downstream of the TPS (ADCP 3), which could be generated by a combination of TPS operation modes and hydrodynamic forcing (*i.e.,* wind and waves) not considered in this study, is not captured by the model. For the three ADCP locations, ebb currents are mainly oriented north-west and flood currents are mainly directed south-east.

4.1.2 Model validation for the year 2019

To assess numerical model reliability and robustness with respect to the current operating mode of the power station, a numerical simulation was performed over a period of a fortnight from August 15 – 28 2019. For this scenario, only water surface measurements were available. Figures 4.a;b;c;d present a comparison between numerical results and measurements at Saint Servan, upstream of the TPS, Saint Suliac and Chatelier Lock respectively (see Figure 1 for tidal gauge locations). The numerical model demonstrated its ability to reproduce satisfactorily the tidal distortion caused by the TPS, as well as to correctly propagate the tidal wave along the estuary, with RMSE below 10 cm (Table 3). Although the model's error on low water levels is slightly higher than error on high water levels, it is still below 10 cm, which is considered satisfactory. Furthermore, the reduction in tidal range inside the estuary is well represented. The model is also able to reproduce the seiche-like oscillations, which are stronger at stations upstream of TPS and Chatelier Lock. Moreover, the amplitude and phase of the M2 and M4 components are well computed, with error below 5 cm and 9° for amplitude and phase respectively (see Table 4).

4.2 Present-day conditions of the Rance estuary

This section focuses on the fortnight's simulation in August 2019. Numerical results were validated for a large dataset of measurements and represent the current mode of plant operation. High and low tides, mean water level and tidal range along the estuary's channel were analyzed. Then, the evolution of the water surface elevation and currents was studied at particular locations in the estuary for both neap and spring tides.

Figure 5.a shows a comparison between spring and neap tide for low water (LWL), high water (HWL) and mean water (MWL) levels along the estuary channel, defined respectively as minimum, maximum and mean water surface elevation during one tide cycle (12 h 25 min). These results suggest that the estuary could be divided into two zones: one from the Chatelier lock to the TPS ($\sim 18\ km$) and one from the TPS downstream to the sea ($\sim 5\ km$). In the latter zone, there is a difference between HW levels (blue lines) at spring and neap tide (and similarly for LW levels, red lines), while, for the same tidal conditions, MW levels (green lines) remain constant. In the former zone, HWL at spring tide is naturally higher than HWL at neap tide (blue lines); however, LW levels (red lines) are nearly coincident. Therefore, MW level (green lines) is not constant between spring tide and neap tide in this zone. In fact, the operating mode of the TPS requires

keeping the yacht harbor upstream of the Chatelier Lock navigable, so a minimum of 2 meters is required in the channel [62], and thus, minimum water level in the estuary channel could not reach its natural value, in contrast to the zone downstream of the TPS. Moreover, LWL, HWL and MWL are always higher in the estuary side than in the sea side. This difference is more significant for LWL, and mainly at spring tide. Consequently, tidal range (Figure 5.b) is decreased in the zone upstream of the TPS by nearly 50% at spring tide and 33% at neap tide compared to the sea-side region.

Water surface elevations and currents were analyzed simultaneously with power station operating modes during a spring tide period (Figures 6.a-h). As seen previously, tidal range is reduced in the estuary and high-frequency oscillations are observed at high and low tide during the Off period of both turbines and sluice gates (T.O. and G.C. stages, Table 1). These oscillations are stronger at the Chatelier Lock, considering the tidal wave reflecting on the upstream boundary condition [63]. Moreover, a lag of $\sim$ 2 hours is observed at high and low tides (and similarly for ebb and flood currents) between Saint Servan (sea) and the other locations along the estuary. After reaching the natural water level maximum (t = 2.4 d), the pump units raise the estuary water level (D.P. phase) to allow a greater drop in the next low tide, maximizing electricity production (D.T. stage). For the same purpose, the high water (resp. low water) slack period lasts for $\sim$1h 20 minutes (resp. $\sim$ 25 minutes), allowing operating modes to be switched from direct pumping to direct turbining (resp. direct turbining to inverse turbining). During spring tide, the TPS can operate in two-way generation, so that the electricity is produced not only during ebb (D.T. stage) but also during flood (I.T. stage). Furthermore, Figures 6.e;f;g show that the TPS amplifies the peak-flood current in the estuary, mainly by the opening of the sluice gates (G.O. stage). This amplification is then reduced toward the estuary's upstream limit (Chatelier Lock). Moreover, flood currents are stronger than ebb-currents on both sea and estuary sides, except near Chatelier Lock (Figure 6.h) where river currents (negative currents) are dominant.

A similar analysis was performed for a neap tide period, as shown in Figures 7.a-h. Since tidal range in the sea side is naturally lower than in spring tide, the operating mode of the TPS is obviously different to ensure electricity production during neap tides as well. Presently, the TPS operates only in one-way generation during this period, so electricity is produced only during ebb (D.T. stage). Thus, in order to meet navigation requirements and ensure a sufficient drop between sea and estuary levels for a long enough time, the direct pumping stage (D.P.) is longer than in spring tide. Consequently, the high-water level in the estuary is clearly higher than in the sea. In addition, the maximum flood-current upstream of the TPS is amplified by pumping

through the turbines and sluice gates rather than the sluice gates only, as is the case at spring tide. However, this amplification is quickly dissipated, since currents at Saint Suliac (~ half the estuary) are weaker than those at Saint Servan (Figures 7.e;g).

4.3 Influence of the tidal power station on hydrodynamics and tide asymmetry

To evaluate the impact of the tidal power station on hydrodynamics and tide asymmetry, three configurations were designed (Table 5) for the fortnight of August 15 – 28 2019. The first (C1) was based on the DEM for 1957 (Figure 2.a). It represents a real configuration of the estuary in the past, specifically before the construction of the dam. The second (C2) is a virtual configuration: the present estuary configuration but without the power station. It was recreated from the DEM for 2018 by removing the dam and smoothing the bottom elevation upstream and downstream of the TPS. The third configuration (C3) represents the present estuary configuration, with the TPS and the DEM for the year 2018 (as presented in section 4.2). Comparison between C1 and C2 scenarios highlights the influence of the bathymetry, spanning ~ 52 years of TPS operation. Comparison between the C2 and C3 configurations emphasises the impact of the TPS over a period of a fortnight. These comparisons are complemented by asymmetry analysis, providing preliminary insights at a larger time scale.

All three numerical simulations were performed using the same hydrological condition (river discharge at Chatelier lock), the same tidal condition (mean sea level and tidal amplitude and phase), and the same physical parameters. The scenarios were first analyzed in terms of hydrodynamic variables along the estuary's main channel. Then, tidal wave propagation and the spatial distribution of currents at neap and spring tide were discussed. Finally, asymmetry parameters were compared for the three configurations to quantify the tidal distortion caused by both artificial hydrodynamic forcing by the TPS and the estuary's morphology.

4.3.1 Hydrodynamic variables

Morphological changes in estuaries may have an important influence on hydrodynamic variables such as low, high, and mean water levels (LWL, HWL, MWL respectively) and tidal range. These quantities were compared along the estuary's channel at spring tide between the configurations without the TPS: C1 with the bathymetry for 1957 and C2 with the bathymetry for 2018 (Figures 8.a-b). Overall, bathymetry does not have a significant impact on the spatial distribution of water level indicators or on tidal range. However, it is

noteworthy that the estuary could be split into two parts in which hydrodynamic variables behave differently. In the first zone, between Chatelier lock and Saint Hubert port ($\sim 6\ km$), the channel is partially uncovered at low tide but keeps the same level at high tide; thus the tidal range is variable and increases according to bottom depth. At spring tide, where differences between low and high tide are large, the limit of tidal range rise occurs approximately at the Saint Hubert port, in contrast to neap tide, where the limit is slightly ($\sim 2\ km$) upstream. In the second zone, from Saint Hubert port to the mouth ($\sim 17\ km$), the channel is always covered, at both neap and spring tides. Moreover, despite some local changes in the channel bottom between 1957 (before the dam construction) and 2018, for instance directly upstream of the TPS, the water level indicators and tidal range do not seem to be influenced. Furthermore, tidal range in this second zone is variable (variation of $\sim 0.5m$ at spring tide and $\sim 0.1m$ at neap tide), as it slightly decreases according to bed position.

As presented in section 4.2, values of LWL, HWL, MWL and tidal range are highly sensitive to dam operations. Comparison of these values for configurations C2 and C3 (respectively with and without the TPS, in Table 5) provides a deeper overview of the influence of the TPS on water level indicators (Figures 8.c-d). Downstream of the dam, the impact of the TPS on water levels and tidal range seems to be negligible, but is more significant upstream. In the last region, the plant amplifies the high-water level (continuous blue line in Figure 8.c) at neap tide by $\sim 10\%$ but maintains approximately the natural maximum level at spring tide. Thus, the dam does not necessarily influence the flooded areas. Low-water level (red line), is strongly increased by the TPS and kept constant along the basin. It nearly reaches the natural mean water level without the structure (green dashed line). Thus, the region between Chatelier lock and Saint Hubert port switches from being an intertidal zone in the configuration without the TPS (C2) to a permanently flooded zone in the configuration with the TPS (C3). In the current study, a mean spring tide cycle was chosen; hence the area between Saint Hubert port and the plant was continually submerged. This behavior might be influenced by the TPS, and especially the area directly downstream of Saint Hubert port (between $8km$ and $12km$ from the Chatelier lock), which may be naturally uncovered during an extreme spring tide but switched to a flooded zone by the plant. Therefore, the dam ensures the continuity and uniformity of water level at low tide along the estuary's channel for the purpose of maintaining navigation to the yacht harbor located upstream of the Chatelier lock. Moreover, mean water levels (green lines) at both spring and neap tidal periods are amplified by the presence of the plant. Furthermore, in the area upstream of the TPS, the difference in tidal range between configurations without and with the dam (Figures 8.b & 8.d) increases according to bed elevation,

peaking at $\sim 5.25m$ at spring tide near Saint Hubert port. Thus, the dam reduces the tidal range by at least $\sim 13\%$ at neap tide and at most $\sim 50\%$ at spring tide.

4.3.2 Tide and current distributions and propagation

The construction of the tidal power station at the estuary's mouth induces a considerable decrease in tidal range, reducing water volume entering and exiting the basin. Also, the Rance dam operates in both one- and two-way generation modes. Therefore, maximum tidal current at both flood and ebb are potentially influenced by the TPS. It is interesting to compare maximum flood and ebb current distributions between scenarios with different bathymetries (C1 and C2 in Table 5), and configurations with and without the dam (C2 and C3 in Table 5), over a spring tide cycle (Figures 9.a-f).

Bathymetry does not seem to have a major impact on maximum flood current distribution (Figures 9.a;b). However, a slight amplification of maximum ebb current occurs in the main channel of the upper estuary from Ton Peak to Saint Servan (Figures 9.d;e). This amplification may be caused by the channel's morphological development over the past 52 years: construction of the TPS to 2018, the main channels upstream of the dam expanded slightly and deepened (Figure 2), allowing faster ebb-current propagation.

Scenarios with and without the TPS showed that the maximum flood current is amplified by the dam directly upstream of the sluice gates, but significantly reduced in the rest of the estuary (Figures 9.b;c). Maximum flood currents upstream of the sluice gates increased from $0.8m/s$ without the TPS to $1.75m/s$ with: *i.e.,* an amplification factor of ~ 2.2. In other words, locally in the region upstream of the dam, the main channel with maximum flood current is controlled by both the modified bathymetry and geometry, and the artificially-induced hydrodynamic forcing by the plant. Nevertheless, the maximum flood current is decreased in the rest of the estuary, from $1.75m/s$ without the TPS to $1.25m/s$ with: *i.e.,* reduction by a factor of ~ 0.7. The same behavior applies for maximum ebb-current: amplification by the TPS directly downstream of the turbines by a factor of ~ 3.1 and reduction in the rest of the estuary by a factor of ~ 0.4. Complementary comparisons of current differences between the three modeled scenarios are given in appendix A.

On the basis of the foregoing remarks, four locations (downstream of TPS, upstream of TPS, Ton peak and Saint Hubert port, Figure 1) were selected to further analyze the influence of dam operating modes on current distribution. The temporal evolution of water surface elevation and currents was analyzed for a mean spring tide on the three scenarios (C1, C2 and C3: Table 5, Figures 10.a-h). As expected, differences are negligible between configurations C1 and C2, with different bottom elevation levels (red and green dashed

lines) on both water surface elevation and currents. Comparison between configurations C2 and C3, without and with the TPS (green dashed line and blue continuous line, respectively) showed that, while the dam does not modify water surface elevation downstream of the TPS (Figure 10.a), it distorts the currents. At this location, peak ebb current is equivalent to peak flood current in the absence of the TPS, while the presence of the TPS leads to a substantially higher peak ebb current than peak flood current. Also, maximum ebb current occurs during the D.T. phase of electricity generation by the turbines, with sluice gates closed. This explains the amplification of maximum ebb current by the TPS directly downstream of the turbines rather than downstream of the whole structure (cf. Figure 9.f). Furthermore, upstream of the TPS, peak ebb current is higher than peak flood current for the configuration without the dam, while the opposite is true for the configuration with the dam (green dashed line and blue line in Figure 10.f). Flood current is maximized by opening the sluice gates during flood (G.O. stage). This is explained on the one hand by the fact that the estuary is filled mostly via sluice gates rather than turbines, and on the other hand sluice gates width ($114m$) is considerably smaller than turbines width ($323m$). Since higher flow through a smaller section induces higher velocity, flood currents upstream of sluice gates are faster than upstream of turbines. Similarly, peak flood currents are significantly greater with the TPS than without. However, this amplification caused by the TPS is remarkably reduced further upstream (for instance, at Ton Peak and Saint Hubert port), as a result of the reduction in tidal range and hence in tidal prism (Figures 10.g;h). In addition, the difference in current magnitude between scenarios with and without TPS also decreases along the estuary, from $0.65m/s$ at Ton Peak for maximum flood current ($0.4m/s$ for maximum ebb current) to $0.25m/s$ at Saint Hubert port for maximum flood current ($0.25m/s$ for maximum ebb current). Moreover, a lag of approximately 2 hours is caused by the TPS for both water elevation and current on the estuary side of the dam. This time lag is related to the elongation of high- and low-water slack periods induced by the operating mode of the turbines to enable efficient electricity generation (see section 4.2). The high-tide slack period changes from 20 minutes for the scenario without the TPS to 1 hour 20 minutes for the scenario with TPS, although the difference is less significant for low-tide slack period. These analyses were carried out over a spring tide period, where the dam operates on two-way generation. Next, a similar analysis was performed over a neap tide period, where the plant is in one-way generation mode (Figures 11.a-h). Overall, the TPS induces a similar impact on water surface elevation and currents during neap and spring tide, except for a few details presented hereafter. On the estuary side of the dam (for instance, upstream of the TPS: Figure 11.b), there was no difference during flood between configurations without (green dashed line) and with the TPS (blue continuous line),

unlike during the spring tidal cycle (Figure 10.b). Thus, at neap tide the plant could operate only on one-way generation, which means electricity is generated only during ebb (D.T. stage) and not during flood as is the case during spring tide. Moreover, to ensure a sufficient water head between the basin and downstream sea level, the D.P. phase is longer during neap than spring tide, resulting in a high tide that is greater than the natural high tide (configuration C2 without TPS). Furthermore, peak flood current upstream of TPS (Figure 11.f) for the configuration with TPS (C3) occurs at the junction between the D.P. phase of the turbines and the G.O. phase of the sluice gates (Table 1) and not during an electricity production phase (D.T. or I.T.) as is the case at spring tide.

To complement tidal current analysis, investigations were conducted on the temporal evolution of flowrate across the section upstream of the TPS (Figure 1) and on tidal prism during a neap-spring tide period for the three simulated scenarios (Figures 12a-d). Over the fortnight period, the TPS reduces discharge both entering (flood) and exiting (ebb) the estuary. Particularly, at spring tide (Figure12.b) maximum flood discharge (ebb discharge) decreases from 10,600m^3/s (−7,500m^3/s at ebb) without the TPS to 7,000m^3/s (−5,000m^3/s at ebb) with the TPS: *i.e.,* a reduction of 34% (33% at ebb). At the neap tide (Figure12.c), the decrease induced by the dam is slightly less: at most 25% at flood and 22% at ebb. It should be borne in mind that the estuary is filled mostly via the sluice gates at spring tide, whereas at neap tide the contributions of sluice gates and turbines are equivalent. Moreover, bathymetry did not seem to have a significant influence on tidal prism (red and green lines in Figure 12.d). However, the presence of the dam (blue line) induces a major decrease in tidal prism, from 1.22×10^8 m^3 without the structure over spring tide (0.6×10^8 m^3 over neap tide) to 0.8×10^8 m^3 with (0.4×10^8 m^3 over neap tide). To evaluate flushing rate in the estuary, tidal prism needs to be compared to the volume of water contained in the basin at high tide, estimated at 1.84×10^8 m^3. Thus, tidal prism accounts for 66% without the TPS at spring tide (33% at neap tide) versus 43% with the TPS at spring tide (22% at neap tide). Theoretical mean residence times in the estuary for scenarios without and with the dam showed that the presence of the TPS could multiply the natural water residence time by a factor of 1.52 at most. Therefore, the presence of the plant causes a lower flushing rate and longer water residence time.

4.3.3 Tide asymmetry parameters

To quantify the distortion and asymmetry of the tidal signal as it crosses the dam and propagates along the basin, two complementary approaches were applied in the three scenarios: C1 configuration from 1957

before TPS construction, C2 configuration of 2018 without the TPS, and C3 configuration of 2018 with the TPS (Table 5).

The first approach focuses on tidal velocity and duration skewness [12]. These parameters ($\gamma_0(u);\gamma_0(\frac{\partial \zeta}{\partial t})$) were computed as the median over a neap-spring tidal period to analyze their spatial distributions in the three scenarios (Figures 13.a-f). Despite the presence of the dam and the morphological evolution in the Rance estuary, tide is flood-dominant in the main channel and ebb-dominant in the secondary channels (Figures 13.a-c). The presence of the power plant slightly decreases the flood-dominance by $5-7\%$ throughout the estuary. Nevertheless, local impacts of the plant on maximum flood and ebb currents (Figures 6; 7 & 9;) also appears in the spatial distribution of velocity skew near the plant: (i) upstream of the sluice gate, the tide is switched from ebb-dominant without the TPS to flood-dominant with, (ii) downstream of the turbines, the tide is switched from flood-dominant without the dam to ebb-dominant with. Complementary comparisons of velocity skew ratios are given in appendix A. Furthermore, in the Rance estuary, with and without the TPS, duration is always longer for falling than rising water. As expected, bathymetry does not induce any significant changes in duration skew. Likewise, the plant does not influence tidal duration asymmetry downstream of the TPS, as seen previously in Figures 6.a & 7.a. Although upstream of the TPS the magnitude of this typical skew is substantially decreased by the TPS, it still maintains the same trend. This behavior could be related to the operating modes of the plant, which tend to extend high tide and low tide slack periods, so that the temporal variation in water surface elevation $\frac{\partial \zeta}{\partial t}$ is equal to zero over this period, in turn decreasing duration asymmetry (cf. Figures 6.b-d & 7.b-d).

The second approach quantifies tidal asymmetry through harmonic analysis using the amplitude ratio $\alpha = a_{M_4}/a_{M_2}$ and phase difference $\beta = (2\phi_{M_2} - \phi_{M_4})$ [11]. This method is suitable for the present case study, as the Rance estuary is a system dominated by the M2 semidiurnal tide [64]. Asymmetry metrics derived from harmonic analysis of both water surface elevation ($\alpha_\zeta;\beta_\zeta$) and currents ($\alpha_u;\beta_u$) were computed over the spring-neap tidal period using the T-TIDE toolbox [61], for the three configurations at six locations: Saint Servan, downstream of TPS, upstream of TPS, Ton peak, Saint Hubert port and Chatelier lock (see Figure 1 for locations and Table 6 for asymmetry metrics). As expected, bathymetry does not have any significant impact on these tidal distortion parameters. For configurations without the TPS (C1 & C2), tide is hardly distorted along the estuary, with α_ζ between 0.048 and 0.05. Moreover, the presence of the plant does not affect asymmetry metrics related to water surface elevation ($\alpha_\zeta;\beta_\zeta$) for stations on the sea side of the dam (Saint Servan and downstream of TPS). However, phase difference related to currents (β_u) in this zone is

modified from 352° without the TPS to 171° with. Hence, location downstream of the TPS switches from flood dominant ($0° < \beta_u < 90°$ or $270° < \beta_u < 360°$) to ebb dominant ($90° < \beta_u < 270°$) [11]. Upstream of the TPS, the presence of the dam modifies the tide from ebb dominant with $\beta_u = 173°$ without the plant to $\beta_u = 355°$ with. Furthermore, Table 6 indicates that the dam induces a substantial decrease in both amplitude ratios α_ζ and α_u by $\sim 70\%$ in the basin side of the plant, but does not modify the flood-dominance behavior of the estuary, except locally near the TPS. These findings are in agreement with the analysis based on Nidzieko and Ralston's parameters [12].

5 Discussion

Investigations carried out based on comparison of hydrodynamic and asymmetry parameters between three scenarios with different DEMs and with presence/absence of the TPS, helped to evaluate the impact of the plant on hydrodynamics in the Rance estuary. It was shown that high tide is slightly increased by the presence of the dam in the estuary side of the plant (Figures 5 & 12). However, this amplification occurs specifically at neap tide. At present, maximum water level upstream of the plant is limited to 12 m [62]: *i.e.,* although during an extreme spring tide where maximum high-water level seaward is above 12 m, the high tide inside the estuary will not exceed 12 m. Hence, the plant effectively protects the estuary from storms and risk of marine flooding. This was also seen in studies of other tidal power plant projects: *e.g.,* the Sihwa Lake TPS [29], the Severn dam, the Flemming Lagoon, the Shoots dam [1] and others [41]. The plant's impact on low tide, however, is more significant. The higher low-water level in the configuration including the TPS (Figures 5 & 12) modifies a large part of the intertidal areas in the basin (present in the scenario without the TPS), which are permanently submerged: *e.g.,* the area between Chatelier lock and Saint Hubert port. This could be directly related to the evolution of the estuary's ecosystems. Kirby & Retière [3] discussed the post-closure environmental effects of the Rance dam and measurements demonstrated that an increase in permanent subtidal area leads to changes in the estuary's ecosystem, with richer biodiversity, increased habitat variety, greater abundance of fish species and greater variety and density for birdlife. Moreover, higher low tide allows navigation to the yacht harbor next to the Chatelier Lock during ebb. As the tide passes through the dam and propagates along the estuary, it becomes more distorted and more asymmetric. This effect has both natural and artificial origins, due to the estuary's morphology and to hydrodynamic forcing by the plant. Simultaneously analyzing tide propagation (Figures 10 & 11), skewness parameters (Figure 13) and

asymmetry (Table 6), shows the area near the dam (~ 1.5km upstream and ~ 0.5km downstream) to be highly sensitive to the presence of the TPS. Amplification of flood current upstream of the sluice gate can cause local bed scouring, which may explain the high erosion rate seen in the same area in Figure 2. Furthermore, with and without the dam, the Rance estuary is mainly flood-dominant with longer duration of falling than rising water and stronger peak flood current than peak ebb current [12, 11, 9, 10]. All this enhances the tendency of residual sediment transport to be in the landward direction: *i.e.,* sediments are carried from the coast toward the estuary [15]. It noteworthy that similar behavior is observed before TPS construction, as confirmed by the C1 results presented in Figure 13. Thus, the plant does not impact the source of sediments present inside the basin. These results are in agreement with measurements performed 15 years after TPS construction, showing that more than 90% of the Rance estuary's sediments came from the sea [65, 24, 27]. In addition, flow velocity away from the TPS zone is substantially lowered by the presence of the dam. This may significantly reduce in the suspended sediment concentrations and thus impact the dynamics of the estuarine turbidity maximum (ETM). Furthermore, prolonging high- and low-water slack periods, due to the presence of the power plant, may impact tidal transport of fine sediment with consequences for the settling, re-suspension and diffusion of fine particles in the water column [18]. However, these interpretations need to be analyzed closely with respect to local conditions of sediment bed composition, since the suspended load carried in the seawater is related to tidal current magnitude if the bed includes unconsolidated sediments [66, 67]. Therefore, the impact of the dam on sedimentation needs further investigation. Furthermore, analysis of tidal prism and flowrate passing through the TPS (Figure 12) showed that the plant significantly reduced flushing rates and hence increases the resident time of water containing suspended sediments and pollutants. This was also reported in other tidal power plant projects [29, 1, 2]. On the other hand, since a greater volume of sediment enters from the sea, reducing the water volume flowing into the estuary during flood might reduce the amount of sediment entering the basin. These interpretations need to be supported by complementary sediment transport simulations or *in-situ* observations.

6 Conclusions

This study presents a detailed analysis of the hydrodynamics of the Rance estuary, influenced by the world's second largest tidal power station. This closed-estuary type exhibits an original configuration due to (i) the presence of the Chatelier lock upstream of the basin and the tidal power station downstream and (ii) the plant's

hybrid tidal energy schemes of ebb-generation and ebb-flood generation. A two-dimensional depth averaged model of the Rance estuary was developed and successfully validated against water level observations and velocity field measurements for many tidal stations throughout the estuary. The model was then applied to simulate the tidally-driven hydrodynamic processes for the present-day conditions of the Rance estuary and two other scenarios featuring: 1) an artificial condition of the estuary without the dam and 2) the historic conditions of the basin (in 1957), before the dam's construction. Then, the simulations were analyzed in terms of basic flow characteristics and tide asymmetry parameters. Numerical results indicated that, in the absence of the TPS, bathymetry does not have any significant impact on hydrodynamics. However, the presence of the dam substantially modifies tidal patterns. The main consequences of the presence of the dam at the estuary mouth can be summarized as follows. (i) A major decrease in tidal range and tidal prism along with the amplification of the estuary's low-water level switches a large part of intertidal zones, which become permanently submerged, which seems to help the estuary's ecosystem. (ii) A limitation of the high-water level inside the estuary up to 12m protects the basin against marine flooding. (iii) There is an overall decrease in tidal currents in the estuary, except upstream of the sluice gates and downstream of the turbines. (iv) Flood currents and ebb currents are locally amplified upstream of the sluice gates and downstream of the turbines respectively. The study also revealed that the Rance estuary, with and without the TPS, is flood-dominant, with a shorter duration of rising than falling water. These findings suggest that sediment transport tends to be in the landward direction: *i.e.,* the plant does not impact the source of sediment present inside the basin. Finally, the study highlights the need to couple hydrodynamics to sediment transport processes to further quantify the impact of the dam on sediment dynamics and morphological changes in the Rance estuary. The effect of sea level rise, estimated to be $\sim$ 10cm between 1957 and 2019 [68], could also be evaluated to have a more consistent overview of the long term evolution of this particular estuarine system.

Acknowledgments

The authors are grateful to Christophe Cochet and Malo Lambert for providing the preliminary version of the model used in this work. Antoine Libaux, Marion Duclercq and Florian Boucard are warmly acknowledged for supplying data from the AGRA Software and feedback on the tidal power station operating modes. We would like to acknowledge Chi-Tuân Pham and Sébastien Bourban for giving advice on the tidal model's validation. Finally, we thank the three reviewers, whose comments and suggestions helped improve and

clarify this manuscript.

Appendices

A Complementary comparisons between the three modeled scenarios

To complement analyses performed in Sections 4.3.2 and 4.3.3 for the three modeled scenarios, plots of current differences and velocity skew ratios are shown in Figures 14 & 15. Scenario C2, corresponding to the bathymetry of 2018 without the tidal power station (see Table 5), is set as reference. Figures 14.a;c show that sediment deposition zones observed near Mordreuc (see Figure 2.c) could significantly impact the velocity magnitude in the main channel, where currents are reduced by $\sim 0.25 m/s$. Figures 14.b;d show that the presence of the dam reduces the current velocities in the estuary main channel by $\sim 0.5 m/s$. However, it amplifies flood (ebb) currents directly upstream of sluice gates (downstream of turbines) by $\sim 1 m/s$.

Velocity skewness ratio depicted in Figure 15.a shows that estuarine morphological changes between 1957 and 2018 near Mordreuc might have switched the ebb-dominance seen in 1957 to flood-dominance in 2018, although this finding may present inaccuracies due to measurement uncertainty in the older maps. Figure 15.b shows that the tidal power station decreases flood-dominance by a factor of ~ 0.9 along the estuary main channel. Moreover, velocity skewness changes are visible in the area surrounding the dam, where the ebb dominance (flood dominance) upstream of the sluice gate (downstream of the turbines) switches to flood dominance (ebb dominance) due to the presence of the TPS.

Notation

$\sum$ = channel cross-sectional area (m^2);

Q = Flow rate (m^3/s);

Q_{river} = River flow rate (m^3/s);

$Q_{turbines}$ = Flow rate passing through turbines (m^3/s);

$Q_{sluices}$ = Flow rate passing through sluice gates (m^3/s);

A, C = Discharge coefficients ($m^{5/2}/s$);

B = Discharge coefficient ($m^{9/4}/s$);

$Q_{\sum_{TPS}}$ = Flow rate passing through section upstream of the TPS(m^3/s);

ζ, WSE = Water surface elevation (m);

T_r = Mean Residence Time (s);

V = Mean volume of water in the system (m^3);

T = Tidal period (s);

b = Return flow factor (-);

TP = Tidal Prism (m^3);

μ_m = The m-th moment about zero ($(m/s)^m$);

$\gamma_0(u)$ = Tidal current asymmetry (-);

$\gamma_0(\frac{\partial \zeta}{\partial t})$ = Tidal duration asymmetry (-);

$a_{M_2}(\zeta)$ = M2 amplitude of water surface elevation (m);

$a_{M_4}(\zeta)$ = M4 amplitude of water surface elevation (m);

$a_{M_2}(u)$ = M2 amplitude of current (m/s);

$a_{M_4}(u)$ = M4 amplitude of current (m/s);

α_ζ = Surface amplitude ratio (-);

α_u = Current amplitude ratio (-);

$\phi_{M_2}(\zeta)$ = M2 phase of water surface elevation (°);

$\phi_{M_4}(\zeta)$ = M4 phase of water surface elevation (°);

$\phi_{M_2}(u)$ = M2 phase of current (°);

$\phi_{M_4}(u)$ = M4 phase of current (°);

β_ζ = Surface phase difference (°);

β_u = Current phase difference (°);

REFERENCES

[1] Xia, J., Falconer, R., and Lin, B. (2010). "Impact of different tidal renewable energy projects on the hydrodynamics processes in the Severn estuary, UK." *Ocean Modelling*, 32, 86–104.

[2] Cornett, A., Cousineau, J., and Nistor, I. (2013). "Assessment of hydrodynamic impacts from tidal power lagoons in the bay of Fundy." *International Journal of Marine Energy*, 1, 33–54.

[3] Kirby, R. and Retière, C. (2009). "Comparing environmental effects of Rance and Severn barrages." *Proceedings of the Institution of Civil Engineers - Maritime Engineering*, 162(1), 11–26.

[4] Stark, J., Smolders, S., Meire, P., and Temmerman, S. (2017b). "Impact of intertidal area characteristics on estuarine tidal hydrodynamics: A modelling study for the Scheldt estuary." *Estuarine, Coastal and Shelf Science*, 198, 138–155.

[5] Stark, J., Meire, P., and Temmerman, S. (2017a). "Changing tidal hydrodynamics during different stages of eco- geomorphological development of a tidal marsh: a numerical modeling study." *Estuarine, Coastal and Shelf Science*, 188, 56–68.

[6] Thurman, H. (1994). *Introductory Oceanography*. NY: Macmillan, New York, $7^{th} edition$.

[7] Sumich, J. (1996). *An Introduction to the Biology of Marine Life*. Dubuque, New York, $6^{th} edition$.

[8] Zhang, W., Cao, Y., Zhu, Y., Zheng, J., Ji, X., Xu, Y., Wu, Y., and Hoitink, A. (2018). "Unravelling the causes of tidal asymmetry in deltas." *Journal of Hydrology*, 564, 588 – 604.

[9] Aubrey, D. and Speer, P. (1985). "A study of non-linear tidal propagation in shallow inlet/estuarine systems Part I: Observations." *Estuarine, Coastal and Shelf Science*, 21, 185–205.

[10] Speer, P. and Aubrey, D. (1985). "A study of non-linear tidal propagation in shallow inlet/estuarine systems Part II: Theory." *Estuarine, Coastal and Shelf Science*, 21, 207–224.

[11] Friedrichs, C. and Aubrey, D. (1988). "Non-linear tidal distortion in shallow well-mixed estuaries: a synthesis." *Estuarine, Coastal and Shelf Science*, 27, 521–454.

[12] Nidzieko, N. and Ralston, K. (2012). "Tidal asymmetry and velocity skew over tidal flats and shallow channels within a macrotidal river delta." *Journal of Geophysical Research*, 117.

[13] Guo, L., Brand, M., Sanders, B. F., Foufoula-Georgiou, E., and Stein, E. D. (2018). "Tidal asymmetry and residual sediment transport in a short tidal basin under sea level rise." *Advances in Water Resources*, 121, 1–8.

[14] Wang, Z., Jeuken, C., and De Vriend, H. (1999). "Tidal asymmetry and residual sediment transport in estuaries." *Delft Hydraulics report Z2749*.

[15] McLachlan, R., Ogston, A., Asp, N., Fricke, A., Nittrouer, C., and Gomes, V. (2020). "Impacts of tidal-channel connectivity on transport asymmetry and sediment exchange with mangrove forests." *Estuarine, Coastal and Shelf Science*, 233.

[16] Mandal, S., Sil, S., Gangopadhyay, A., Jena, B., and Venkatesan, R. (2020). "On the nature of tidal asymmetry in the gulf of Khambhat, Arabian sea using HF radar surface currents." *Estuarine, Coastal and Shelf Science*, 232, 106–481.

[17] Bolle, A., Bing Wang, Z., Amos, C., and De Ronde, J. (2010). "The influence of changes in tidal asymmetry on residual sediment transport in the western Scheldt." *Continental Shelf Research*, 30, 871–882.

[18] Dronkers, J. (2005). *Dynamics of coastal systems*, Vol. 25. World Scientific.

[19] Vellinga, N., Hoitink, A., van der Vegt, M., Zhang, W., and Hoekstra, P. (2014). "Human impacts on tides overwhelm the effect of sea level rise on extreme water levels in the Rhine–Meuse delta." *Coastal Engineering*, 90, 40 – 50.

[20] Hoitink, A. J. F., Hoekstra, P., and van Maren, D. S. (2003). "Flow asymmetry associated with astronomical tides: Implications for the residual transport of sediment." *Journal of Geophysical Research: Oceans*, 108(C10).

[21] Evans, G. and Prego, R. (2003). "Rias, estuaries and incised valleys." *Marine geology*, 196, 171–175.

[22] Pelc, R. and Fujita, R. (2002). "Renewable energy from the ocean." *Marine Policy*, 26, 471–479.

[23] EDF (2020). "L'usine marémotrice de la Rance", <https://www.edf.fr/groupe-edf/produire-une-energie-respectueuse-du-climat/accelerer-le-developpement-des-energies-renouvelables/usine-maremotrice-rance/decouvrir-et-comprendre>.

[24] Bonnot-Courtois, C., Caline, B., L'Homer, A., and Le Vot, M. (2002). *Mont-Saint-Michel Bay and the Rance estuary*. Bull. Centre Rech. Elf Explor.

[25] Guesmia, M. (2001). "Régime hydrodynamique et sédimentaire de l'estuaire de la Rance" (June).

[26] Guesmia, M., Cheviet, C., and Macur, O. (2001). "Modélisation hydrosédimentaire de l'estuaire de la Rance – modélisation courantologique bidimensionnelle" (May).

[27] Thiebot, J. (2008). "Numerical modelling of the processes which govern the formation and the degradation of muddy massifs -application to the Rance estuary and to the Sèvre Niortaise river banks." Ph.D. thesis, Sciences of the Universe, AgroParisTech,

[28] Chevé, J. and Le Noc, S. (2018). "VibRance : Evaluation des impacts bacteriologiques dans l'estuaire de la Rance" (May).

[29] Young, H., Kyeong, O., and Byung, H. (2010). "Lake Sihwa tidal power plant project." *Ocean Engineering*, 37, 454–463.

[30] Cornett, A., Durand, N., and Serrer, M. (2010). "3-D modelling and assessment of tidal current resources in the bay of Fundy, Canada." *Proc. 3rd Int. Conf. on Ocean Energy*.

[31] Hydrelect (2012). "La turbine Kaplan." *hydrelect.info*.

[32] Charlier, R. (2007). "Forty candles for the Rance river TPP tides provide renewable and sustainable power generation." *Renewable and Sustainable Energy Reviews*, 11, 2032–2057.

[33] Trubert, B. and S., I. (2016). "Estuaire de la rance de l'écluse du Chatelier à la mer" (june).

[34] EDF (2018). "Rapport de fin d'intervention de la campagne 2018" (june).

[35] SHOM (2015). "Dalles bathymétriques fra-14581 et fra-14582" (March).

[36] Lane, S. N. (1998). "Hydraulic modelling in hydrology and geomorphology: a review of high resolution approaches." *Hydrological Processes*, 12(8), 1131–1150.

[37] Vreugdenhil, C. B. (2013). *Numerical methods for shallow-water flow*, Vol. 13. Springer Science & Business Media.

[38] Xie, D., Gao, S., Wang, Z. B., Pan, C., Wu, X., and Wang, Q. (2017). "Morphodynamic modeling of a large inside sandbar and its dextral morphology in a convergent estuary: Qiantang estuary, China." *Journal of Geophysical Research: Earth Surface*, 122(8), 1553–1572.

[39] Angeloudis, A. and Falconer, R. A. (2017). "Sensitivity of tidal lagoon and barrage hydrodynamic impacts and energy outputs to operational characteristics." *Renewable Energy*, 114, 337 – 351.

[40] García-Oliva, M., Djordjević, S., and Tabor, G. R. (2017). "The impacts of tidal turbines on water levels in a shallow estuary." *International Journal of Marine Energy*, 19, 177 – 197.

[41] Neil, S., Angeloudis, A., Robins, P., Walkington, I., Ward, S., Masters, I., Lewis, M., Piano, M., Avdis, A., Piggot, M., Aggidis, G., Evans, P., Adcock, T., Ẑidonus, A., Ahmadian, R., and Falconer, R. (2018). "Tidal range energy resource and optimization - Past perspectives and future challenges." *Renewable Energy*, 127, 763–778.

[42] Bi, Q. and Toorman, E. (2015). "Mixed-sediment transport modelling in Scheldt estuary with a physics-based bottom friction law." *Ocean Dynamics*, 65(4), 555–587.

[43] Brown, J. and Davies, A. (2010). "Flood/ebb tidal asymmetry in a shallow sandy estuary and the impact on net sand transport." *Geomorphology*, 114(3), 431–439.

[44] Santoro, P., Fossati, M., and Piedra-Cueva, I. (2013). "Study of the meteorological tide in the Río de la Plata." *Continental Shelf Research*, 60, 51–63.

[45] Van, L. A. (2012). "Numerical modelling of sand-mud mixtures settling and transport processes: application to morphodynamic of the Gironde estuary (france)." Ph.D. thesis, Université Paris-Est, Université Paris-Est.

[46] Orseau, S., Huybrechts, N., Tassi, P., Pham Van Bang, D., and Klein, F. (2020). "Two-dimensional modeling of fine sediment transport with mixed sediment and consolidation: Application to the Gironde estuary, france." *International Journal of Sediment Research*.

[47] Bizien, H. and Soenen, A. (2012). "Mesures de courants aux abords de la centrale marémotrice de la rance" (June).

[48] Barton, A. (2019). "Bluekenue enhancements from 2014 to 2019." *Proceedings of the 26th TELEMAC-MASCARET User Conference*, 1–9.

[49] Cochet, C. and Lambert, M. (2017). "The Rance tidal power plant model." *Proceedings of the 24th TELEMAC-MASCARET User Conference*, 191–196.

[50] Achilleos, G. (2011). "The inverse distance weighted interpolation method and error propagation mechanism – creating a DEM from an analogue topographical map." *Journal of Spatial Science*, 56(2), 283–304.

[51] Egbert, G. and Svetlana, Y. (2002). "Efficient inverse modeling of barotropic ocean tides." *Journal of Atmospheric and Oceanic Technology*, 19.2, 183–204.

[52] Angeloudis, A., Falconer, R., Bray, S., and Ahmadian, R. (2016). "Representation and operation of tidal energy impoundments in a coastal hydrodynamic model." *Renewable Energy*, 99, 1103–1115.

[53] Libaux, A. and Drouot, J. (2020). "Remplacement de la conduite de la Rance - Présentation du package RANG 3-AGRA Version 0.7.0" (July).

[54] Bellman, R. (1954). "The theory of dynamic programming." *Bulletin of the American Mathematical Society*, 60, 503–515.

[55] Telemac-Mascaret Modelling System (2018). *TELEMAC-2D User's Manual*.

[56] Davis, R. and Fitzgerald, D. (2004). *Beaches and Coasts*. Blackwell Science, Malden, MA.

[57] De Brauwere, A., De Brye, B., Blaise, S., and Deleersnijder, E. (2011). "Residence time, exposure time and connectivity in the Scheldt estuary." *Journal of Marine Systems*, 84, 85–95.

[58] Sanford, L., Boicourt, W., and Rives, S. (1992). "Model for estimating tidal flushing of small embayments." *Journal of Waterway, Port, Coastal, and Ocean Engineering*, 118, 635–65.

[59] Marsooli, R., Orton, P., Fitzpatrick, J., and Smith, H. (2018). "Residence time of a highly urbanized estuary: Jamaica bay, New York." *Journal of Marine Science and Engineering*, 6, 44.

[60] Monsen, N., Cloern, J., Lucas, L., and Monismith, S. (2002). "A comment on the use of flushing time, residence time, and age as transport time scales." *Limnol. Oceanogr.,*, 47, 1545–1553.

[61] Pawlowicz, R., Beardsley, B., and Lentz, S. (2002). “Classical tidal harmonic analysis including error estimates in MATLAB using T-TIDE.” *Computers and Geosciences*, 28, 929–937.

[62] Caude, G., Clément, P., Pillet, D., and Vindimian, E. (2017). *Gestion sédimentaire de l’estuaire de la Rance* (in French).

[63] Duclercq, M. (2020). “La Rance: Impact du nouveau mode dechargeur sur l’intumescence dans l’estuaire en cas de declenchement" (February).

[64] Bauer, H. A. (1993). “A world map of tides.” *Geographical Review*, 23, 259–270.

[65] LCHF (1982). “Étude sédimentologique de l’estuaire de la Rance". (in French).

[66] Van Rijn, L. (1984). “Sediment transport, Part II: Suspended load transport.” *Journal of Hydraulic Engineering*, 110, 1613–1641.

[67] Falconer, R. and Chen, Y. (1991). “An improved representation of flooding and drying and wind stress effects in a 2D tidal numerical model.” *Institution of Civil Engineers*, 2, 659–672.

[68] SHOM (2020). “Permanent Service for Mean Sea Level", <https://www.psmsl.org/data/obtaining/stations/454.php>.

List of Tables

TABLE 1. Operating modes of sluice gates and turbines.

Structure	Sluice gates		Turbines					
Operating mode	G.O.	G.C.	F.O.	D.O.	I.T.	D.T.	D.P.	T.O.
Definition	Gates Open	Gates Close	Filling On	Draining On	Inverse Turbining	Direct Turbining	Direct Pumping	Turbines Off
Tidal phase	Flood Ebb	Flood Ebb	Flood	Ebb	Flood	Ebb	Flood	Flood Ebb

TABLE 2. Turbines and sluice gates flowrate parameters

Tidal phase	A	B	C	$\zeta_{downstream}$
Flood	-132.61	-948.22	-900.9	$\zeta_{estuary}$
Ebb	161.98	960.96	912.73	max(1,ζ_{sea})

TABLE 3. Root Mean Square Error (RMSE) computation between numerical results and measurements for years 2012 and 2019.

Data set year	2012			2019			
RMSE	ADCP 1	ADCP 2	ADCP 3	Saint Servan	upstream of TPS	Saint Suliac	Chatelier Lock
Water Surface Elevation (cm)	8.11	8.13	5.04	6.22	9.12	8.74	8.08
High Water Level (cm)	4.44	4.46	3.08	5.42	4.38	4.24	4.05
Low water Level (cm)	2.41	2.26	2.05	9.58	8.24	8.78	—
Current magnitude(m/s)	0.1	0.18	0.2		—		
Current direction (°)	12	11	8		—		

TABLE 4. Computation of harmonics amplitude and phase errors based on tidal constituents of water surface elevation between numerical results and measurements for year 2019. All results were obtained with the T-TIDE toolbox [61] .

Tidal constituents	M2		M4	
Error on	Amplitude (cm)	Phase (°)	Amplitude (cm)	Phase (°)
Saint Servan	3.02	3	2.41	8
upstream of TPS	4.21	4	3.89	9
Saint Suliac	4.15	4	3.77	9

TABLE 5. Modeling scenarios

Name	Bathymetry	Type
C1	1957	Without power station
C2	2018	Without power station
C1	2018	With power station

TABLE 6. Asymmetry metrics derived from the harmonic analysis of water surface elevation (ζ) and current (u) at six selected positions along the estuary (Figure 1 for locations) for the three modeling scenarios (Table 5). All results were obtained with the T-TIDE toolbox [61] .

Scenarios	C1, B1957 Before TPS				C2, B2018 Without TPS				C3, B2018 With TPS			
Variables	Water Surface Elevation		Current		Water Surface Elevation		Current		Water Surface Elevation		Current	
Locations	$\alpha_\zeta(-)$	$\beta_\zeta(^\circ)$	$\alpha_u(-)$	$\beta_u(^\circ)$	$\alpha_\zeta(-)$	$\beta_\zeta(^\circ)$	$\alpha_u(-)$	$\beta_u(^\circ)$	$\alpha_\zeta(-)$	$\beta_\zeta(^\circ)$	$\alpha_u(-)$	$\beta_u(^\circ)$
Saint Servan	0.048	82	0.1	23	0.049	82	0.1	24	0.05	83	0.1	14
Downstream of TPS	0.05	106	0.09	350	0.05	107	0.092	352	0.047	110	0.093	171
Upstream of TPS	0.051	85	0.096	175	0.05	85	0.1	173	0.013	175	0.024	355
Ton Peak	0.05	90	0.098	50	0.05	90	0.096	48	0.015	171	0.028	290
Saint Hubert Port	0.05	126	0.1	281	0.05	128	0.098	285	0.012	170	0.021	287
Chatelier Lock	0.08	88	0.15	197	0.07	87	0.14	196	0.017	169	0.031	157

List of Figures

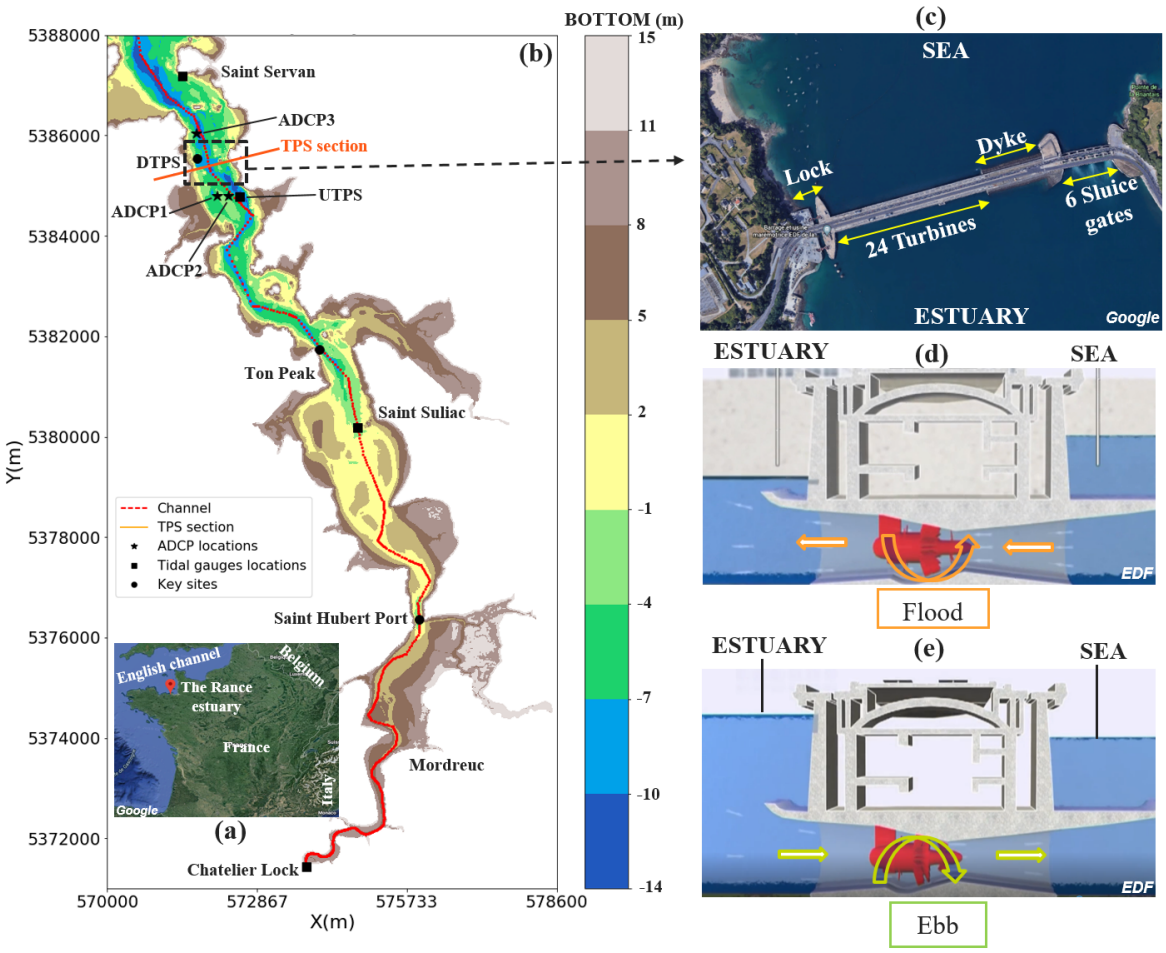

Fig. 1. The Rance estuary: (a) location map, (b) zoom on the estuary with filled contours of 2018 bathymetry, (c) zoom on the tidal power station (TPS). Vertical plan view of the turbine generators during (d) flood and (e) ebb. Sketches (d) and (e) © EDF (modified).

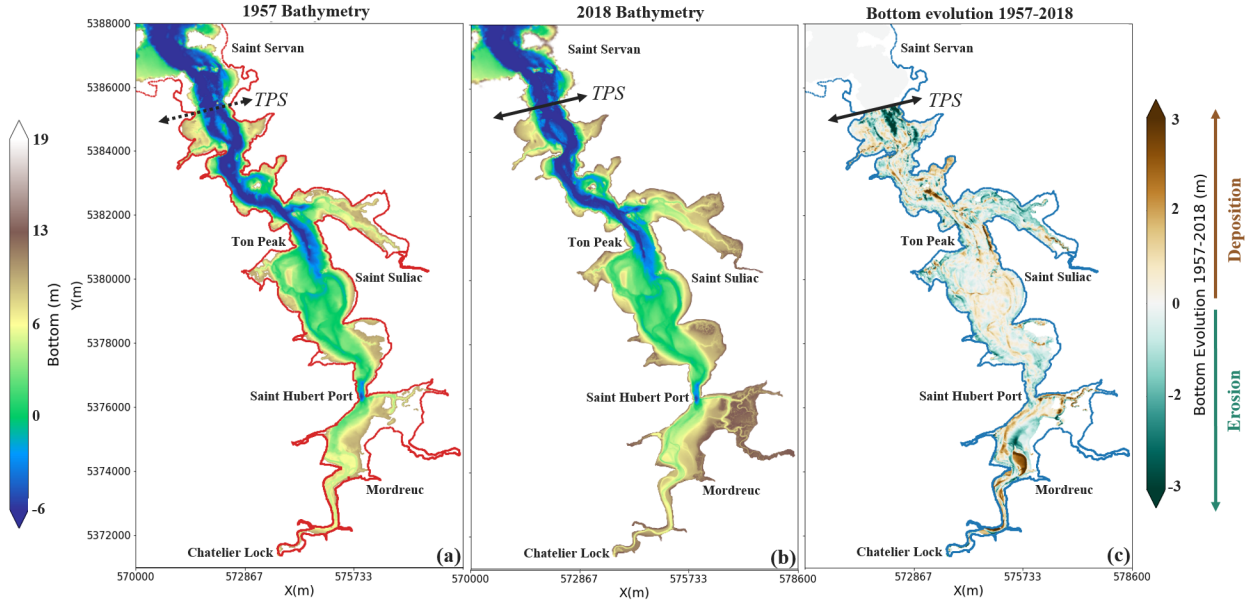

Fig. 2. (a) Bathymetry of 1957 (before the construction of the tidal power station). Blank area represents the zones where the bathymetry is less reliable. (b) Bathymetry of 2018. Bathymetry evolution between 1957 and 2018.

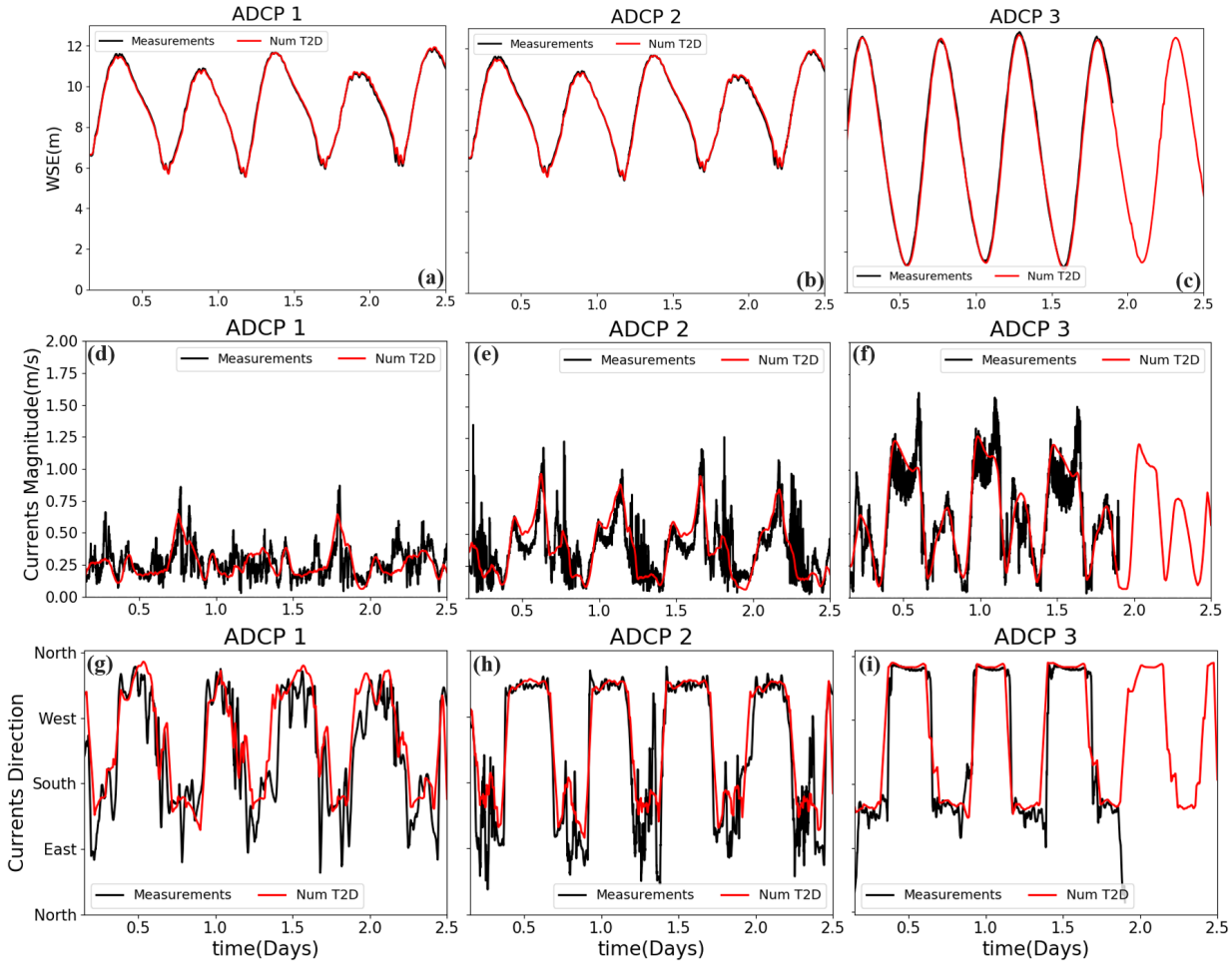

Fig. 3. Comparison of numerical results and measured data from data set of 2012: water surface elevation, current magnitude and current direction respectively at positions (a;d;g) ADCP 1 upstream of the turbines, (b;e;h) ADCP 2 upstream of the sluice gates and (c;f;i) ADCP 3 downstream of the tidal power station (see locations in Figure 1).

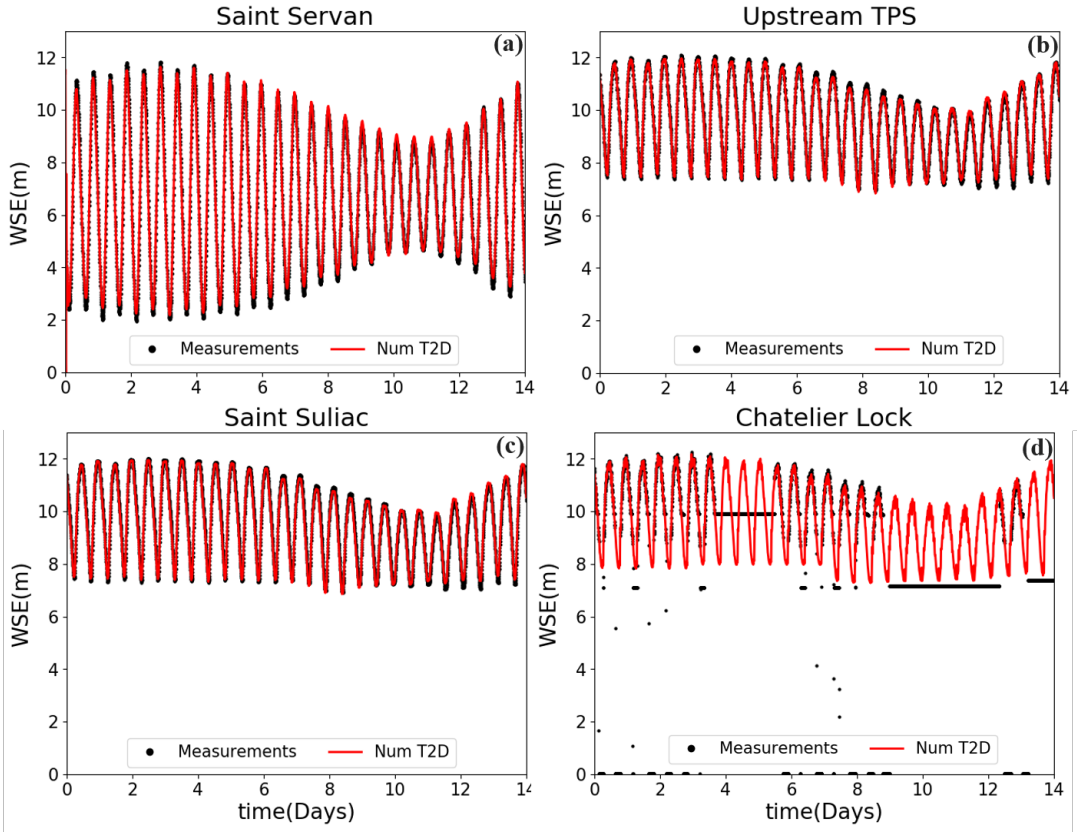

Fig. 4. Comparison of water surface elevation between numerical and measured data, over a period of a fortnight from August 15 to 28 2019, at (a) Saint Servan, (b) upstream of tidal power station, (c) Saint Suliac and (d) Chatelier lock (see locations in Figure 1). Red lines and black dots indicate respectively numerical results and measured data. The measurements are not reliable at low tide at Chatelier Lock station because of technical difficulties of the gauge.

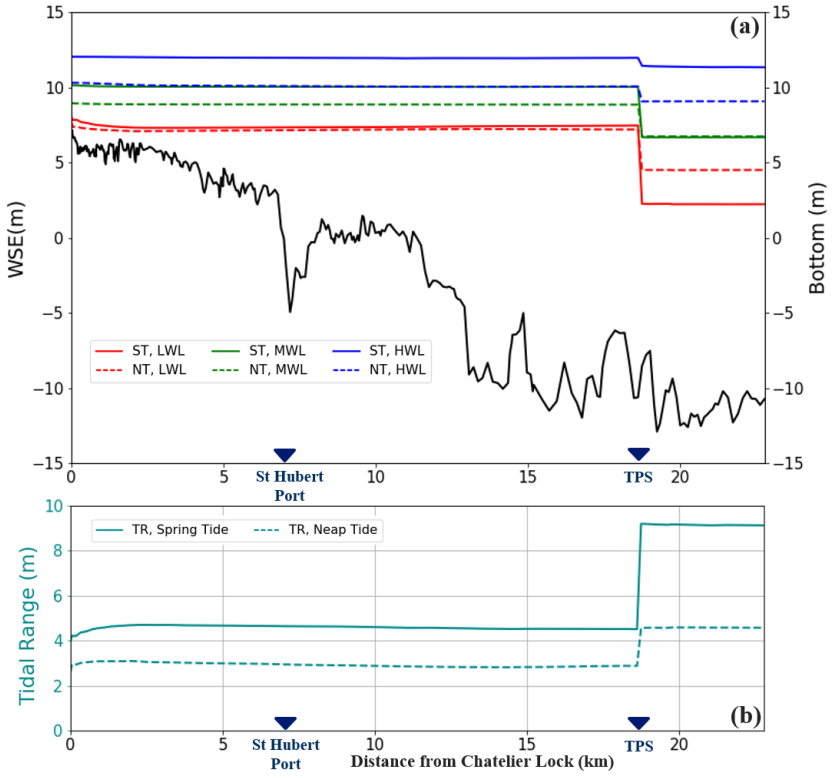

Fig. 5. Comparison of (a) low, mean, high water levels and (b) tidal range at neap and spring tide along the estuary channel (see Figure 1 for channel position). The black line indicates bed elevation.

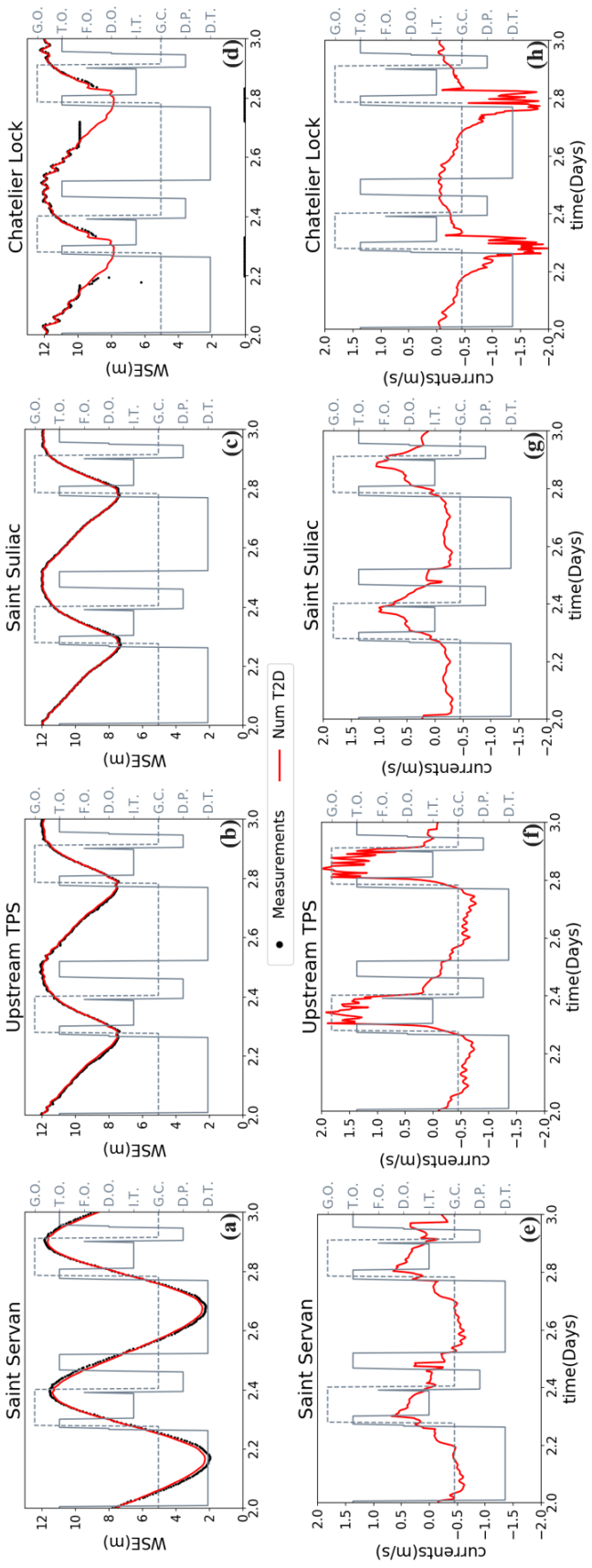

Fig. 6. Hydrodynamic variables during spring tidal period: water surface elevation and currents respectively at locations (a;e) Saint Servan, (b;f) upstream of TPS, (c;g) Saint Suliac and (d;h) Chatelier Lock. Black dots and red lines indicate respectively measurements and numerical simulation. Gray solid- and dashed-lines represent operating modes of the TPS (see Table 1).

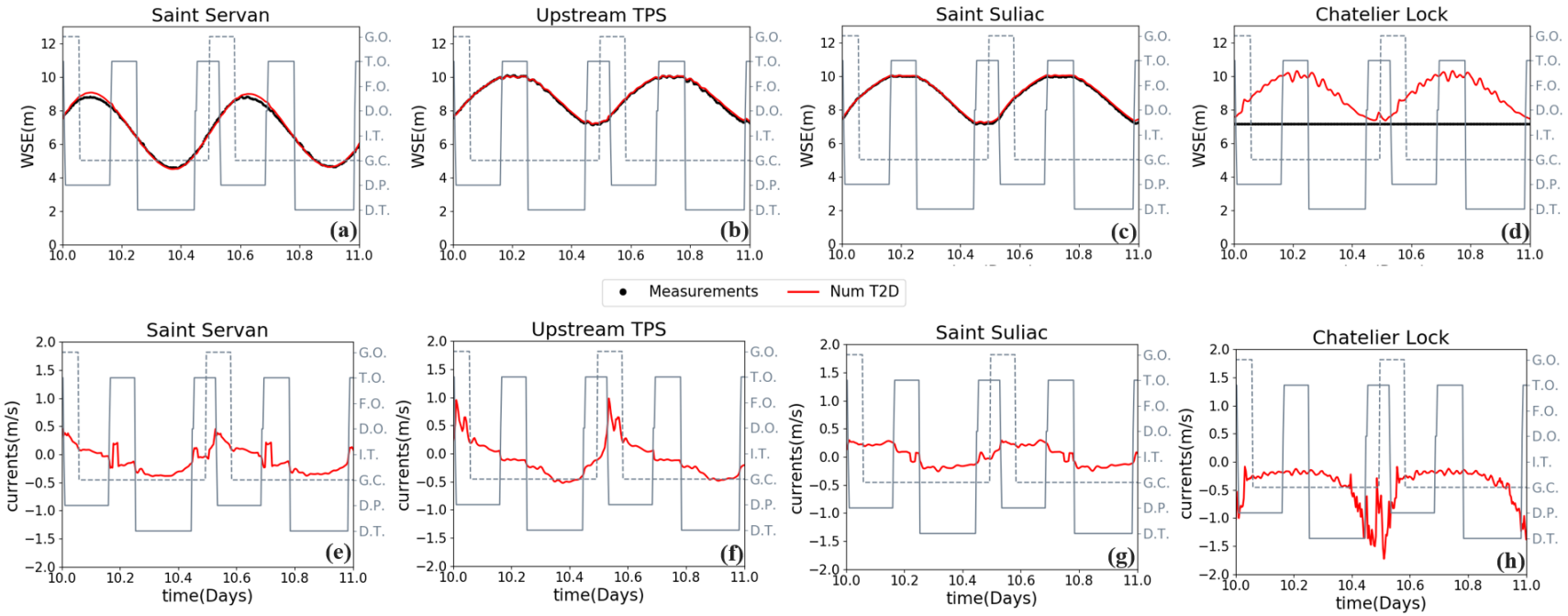

Fig. 7. Hydrodynamic variables during neap tidal period: water surface elevation and currents respectively at locations (a;e) Saint Servan, (b;f) upstream of TPS, (c;g) Saint Suliac and (d;h) Chatelier Lock. Black dots and red lines indicate respectively measurements and numerical simulation. Gray solid- and dashed-lines represent operating modes of the TPS (see Table 1).

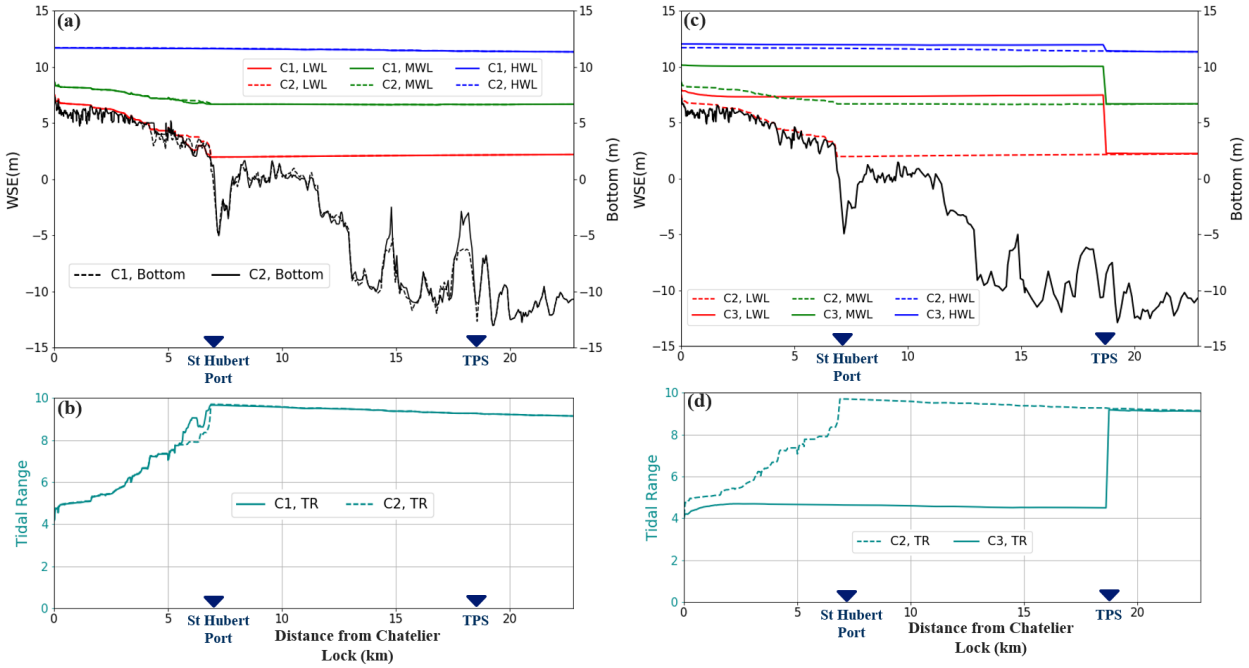

Fig. 8. Spatial comparison of hydrodynamic parameters between configurations C1, C2 and C3 along the estuary channel at spring tide (see Figure 1 for channel location). (a;b) For low, mean, high water levels and tidal range respectively between configurations C1 and C2. (c;d) For low, mean, high water levels and tidal range respectively between configurations C2 and C3. Black dashed- and solid-lines indicate bed elevation in 1957 and 2018 respectively.

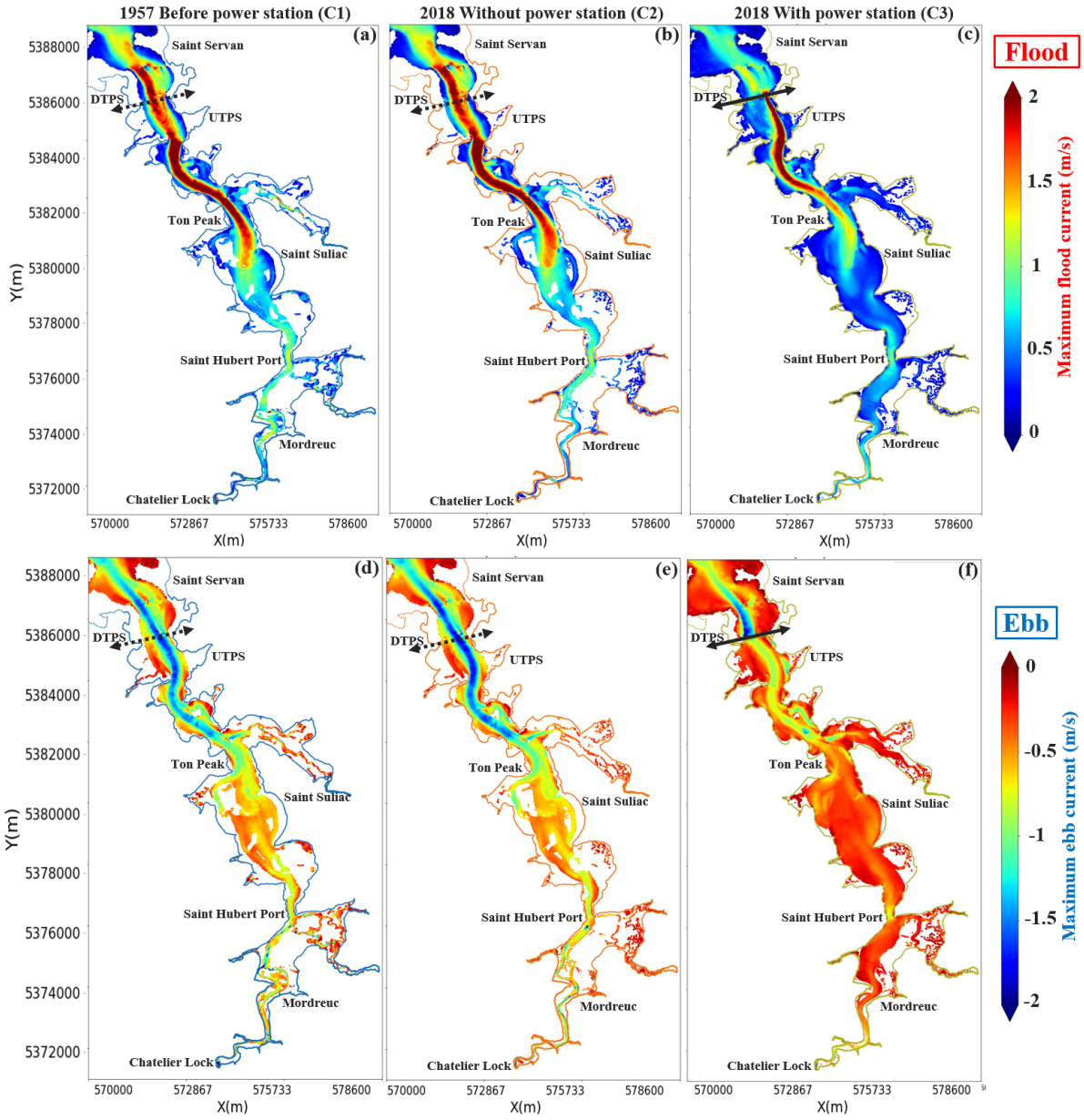

Fig. 9. Spatial distribution of (a;b;c) maximum flood currents and (d;e;f) maximum ebb currents for the three studied scenarios respectively. Dry zones at ebb are blanked.

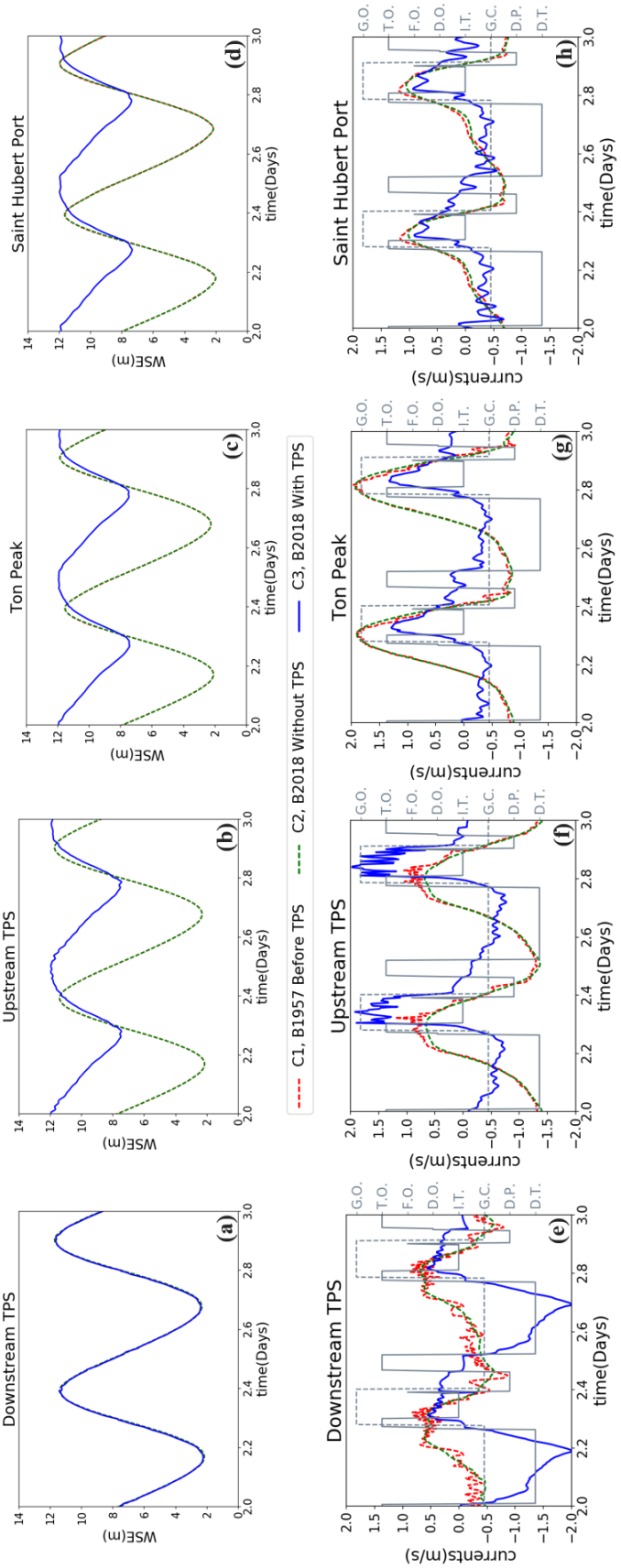

Fig. 10. Hydrodynamic variables of the three scenarios during spring tidal period: water surface elevation and currents respectively at locations (a;e) downstream of TPS, (b;f) upstream of TPS, (c;g) Ton Peak and (d;h) Saint Hubert Port. Gray solid- and dashed-lines represent operating modes of the TPS (see Table 1).

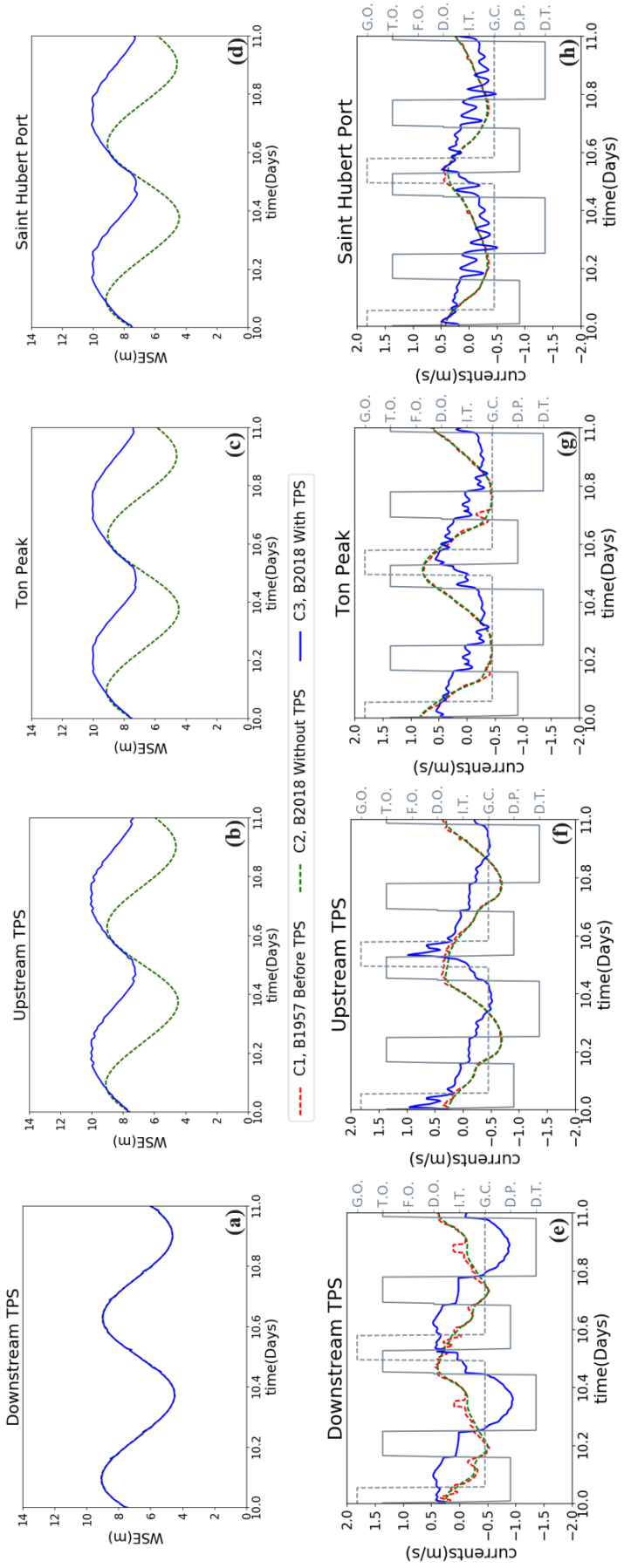

Fig. 11. Hydrodynamic variables of the three scenarios during neap tidal period: water surface elevation and currents respectively at locations (a;e) downstream of TPS, (b;f) upstream of TPS, (c;g) Ton Peak and (d;h) Saint Hubert Port. Gray solid- and dashed-lines represent operating modes of the TPS (see Table 1).

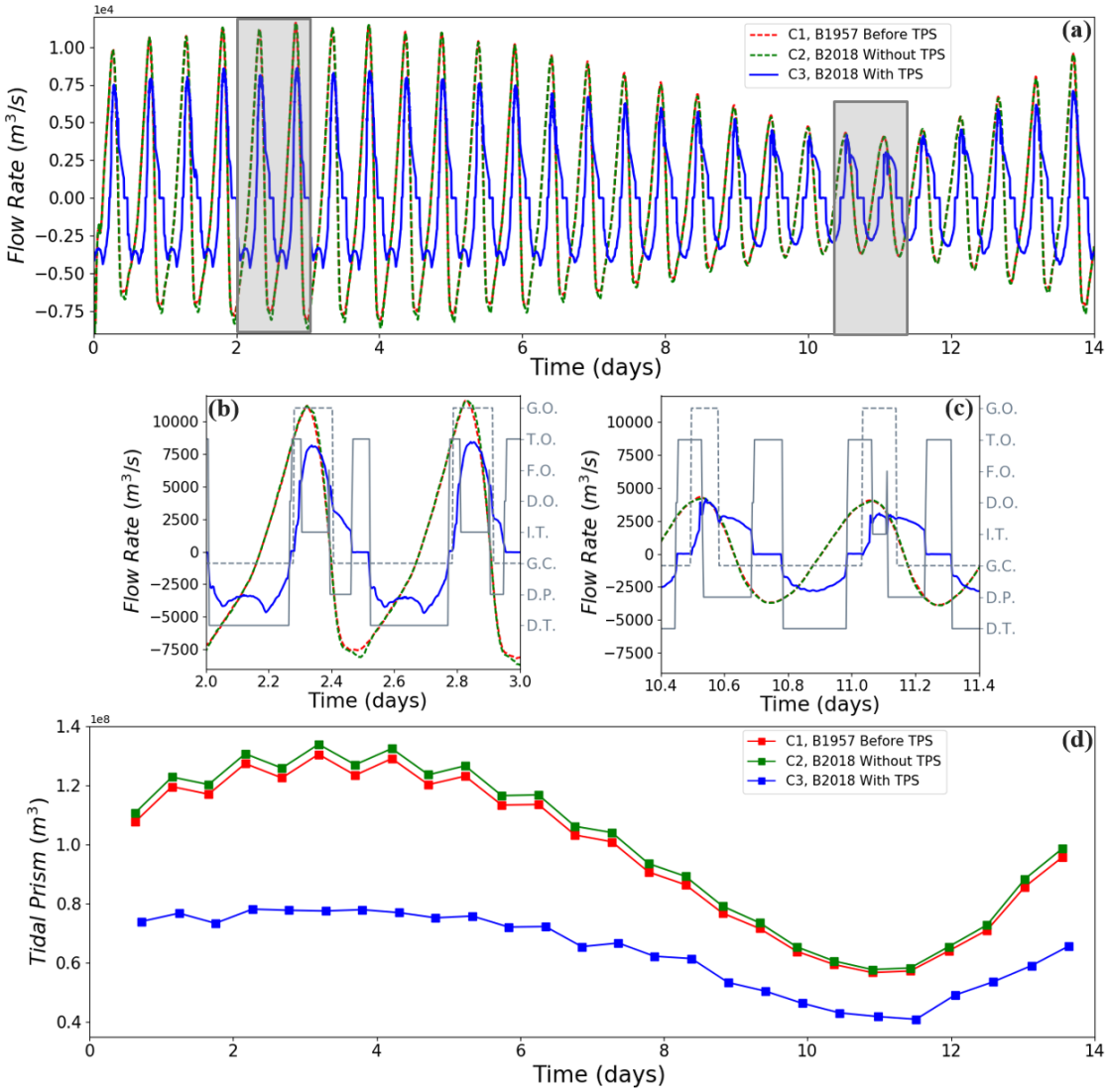

Fig. 12. Temporal evolution at TPS section of (a) flowrate during a fortnight period, (b) zoom on flowrate during spring tide (two-way generation mode), (c) zoom on flowrate during neap tide (one-way generation mode) and (d) tidal prism for the three scenarios. (see Figure 1 for section location).

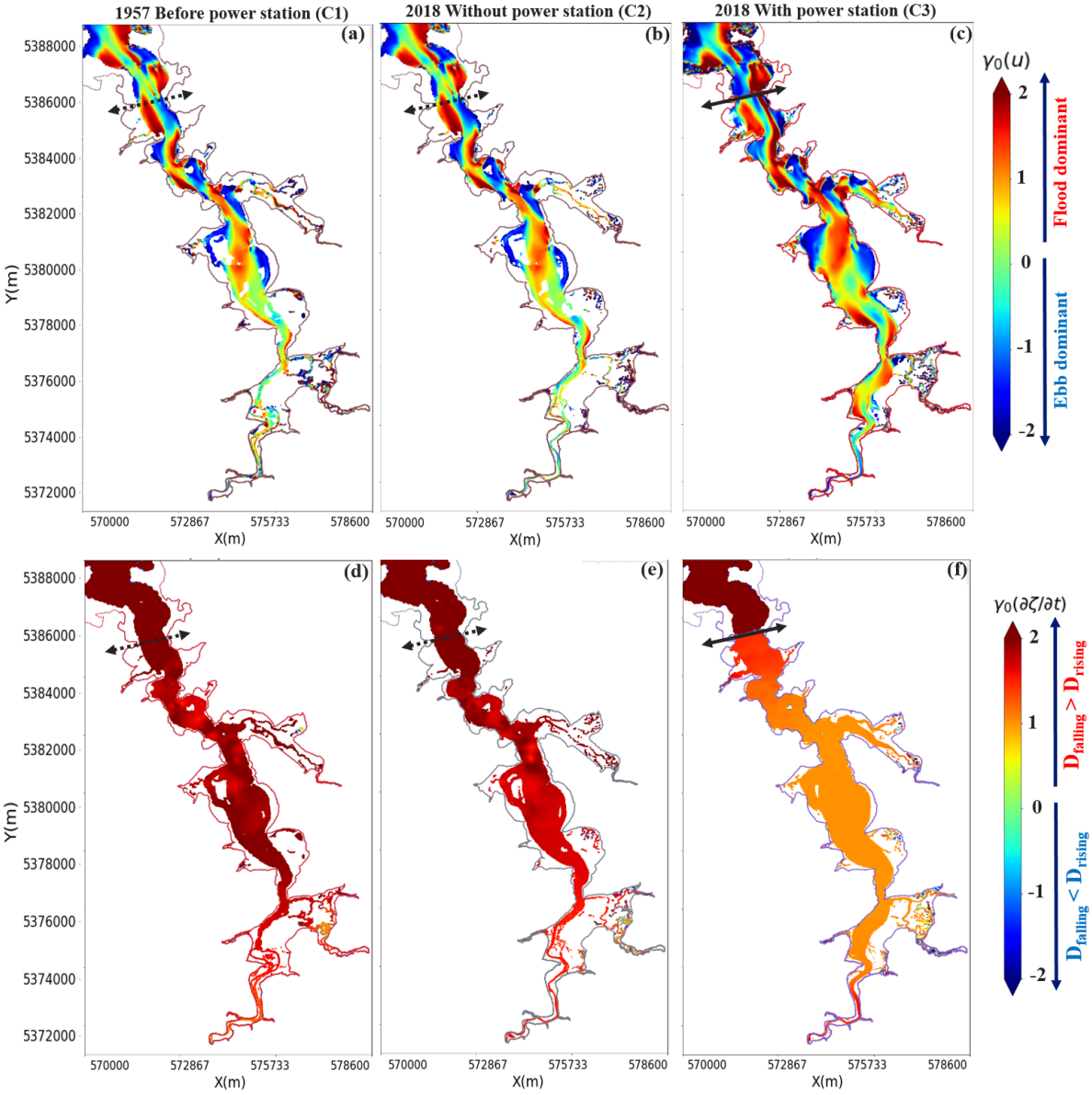

Fig. 13. Spatial distribution of (a;b;c) velocity skewness parameter $\gamma_0(u)$ and (d;e;f) tidal duration asymmetry parameter $\gamma_0(\frac{\partial \zeta}{\partial t})$ for the three scenarios respectively. Dry zones at ebb are blanked.

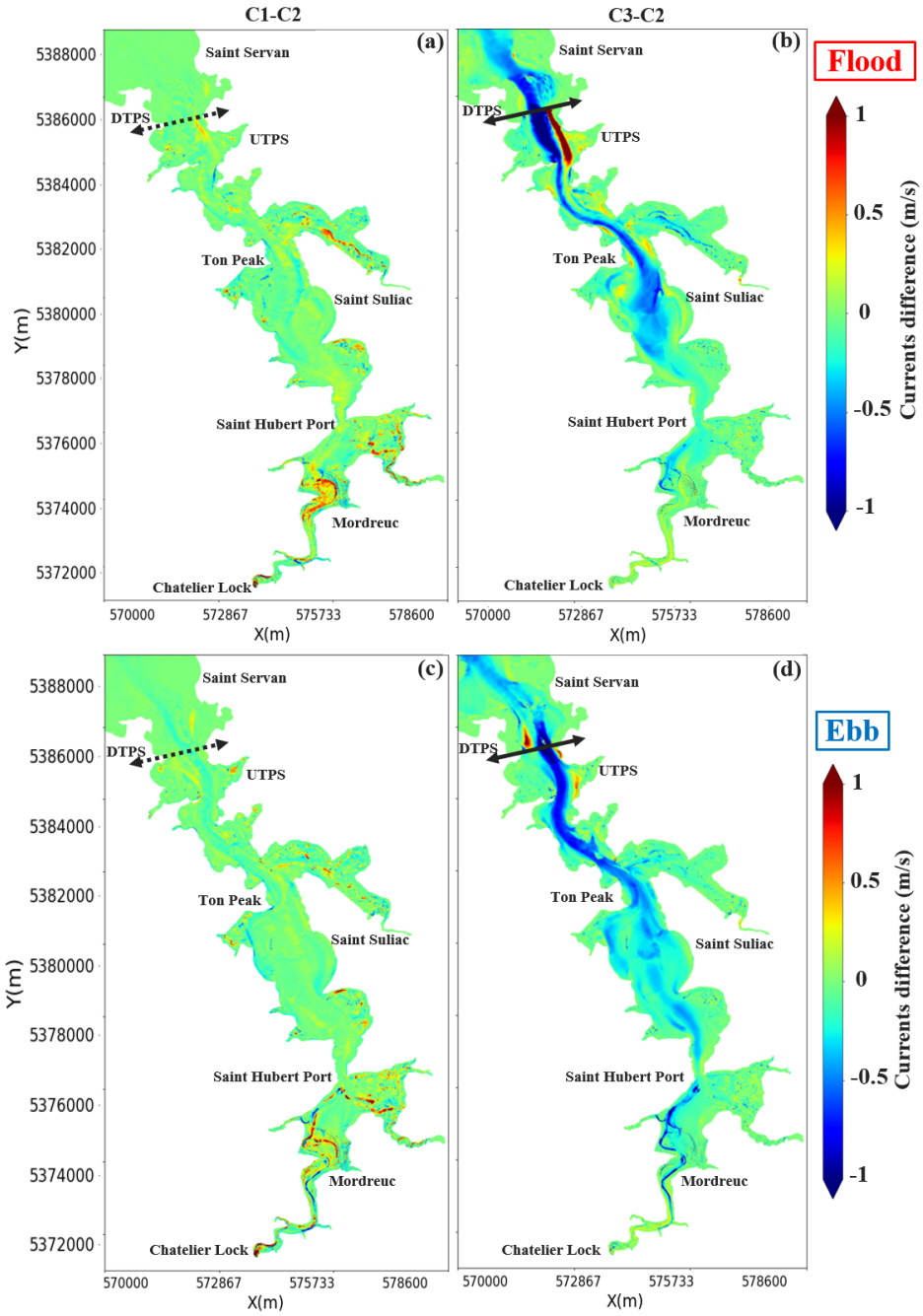

Fig. 14. Spatial distribution of (a;b) maximum flood current differences and (c;d) maximum ebb current differences between the three modeled scenarios. The reference scenario is C2 (see Table 5). Positive (negative) current differences mean flow acceleration (deceleration).

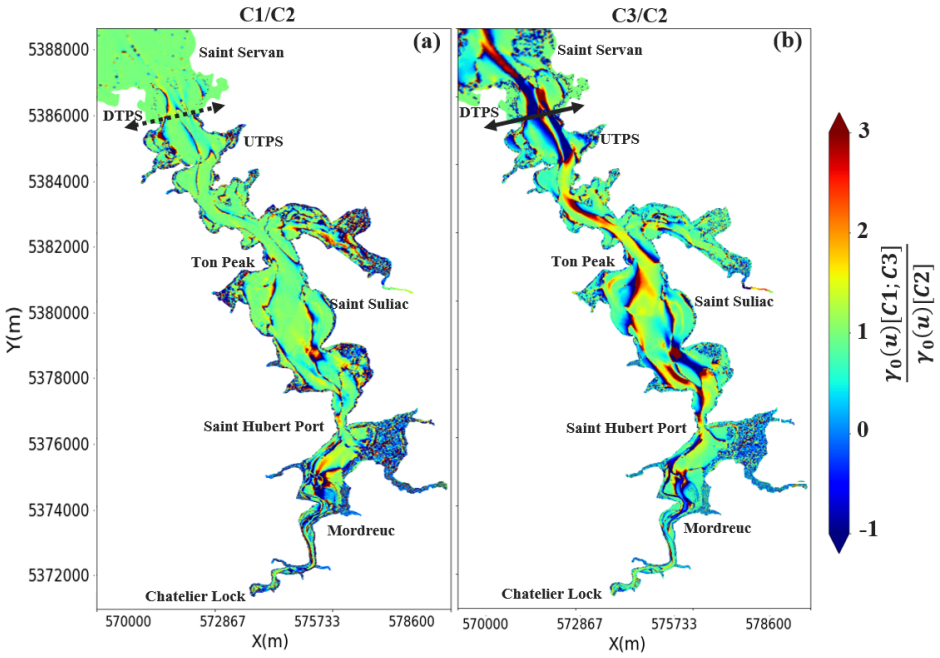

Fig. 15. Spatial distribution of velocity skewness ratio between (a) C1 and C2 scenarios and (b) C3 and C2 scenarios. The reference scenario is C2 (see Table 5). If velocity skewness ratio is negative, both C1 and C3 scenarios switch the flood (ebb) dominance to ebb (flood) dominance. The flood dominance is amplified (decreased) for both C1 and C3 scenarios when the velocity skewness ratio is larger than one (between zero and one). The ebb dominance is amplified (decreased) for both C1 and C3 scenarios when the velocity skewness ratio is between zero and one (larger than one).